Periodically driven Rydberg chains with staggered detuning

Bhaskar Mukherjee ⬤,[1] Arnab Sen ⬤,[2] and K. Sengupta ⬤[2]

[1]*Department of Physics and Astronomy, University College London, Gower Street, London WC1E 6BT, United Kingdom*
[2]*School of Physical Sciences, Indian Association for the Cultivation of Science, Jadavpur, Kolkata 700032, India*

We study the stroboscopic dynamics of a periodically driven finite Rydberg chain with staggered (Δ) and time-dependent uniform [$\lambda(t)$] detuning terms using exact diagonalization. We show that at intermediate drive frequencies (ω_D), the presence of a finite Δ results in violation of the eigenstate thermalization hypothesis (ETH) via clustering of Floquet eigenstates. Such clustering is lost at special commensurate drive frequencies for which $\hbar\omega_d = n\Delta$ ($n \in Z$) leading to restoration of ergodicity. The violation of ETH in these driven finite-sized chains is also evident from the dynamical freezing displayed by the density-density correlation between Rydberg excitations at even sites of the chain for specific ω_D. Such a correlator exhibits stable oscillations with perfect revivals when driven close to the freezing frequencies for initial all spin-down ($|0\rangle$) or Neel ($|\mathbb{Z}_2\rangle$, with up spins on even sites) states. In contrast, for the $|\bar{\mathbb{Z}}_2\rangle$ (time-reversed partner of $|\mathbb{Z}_2\rangle$) initial state, we find complete absence of such oscillations leading to freezing for a range of ω_D; this range increases with Δ. We also study the properties of quantum many-body scars in the Floquet spectrum of the model as a function of Δ and show the existence of mid-spectrum scars at large Δ which do not have overlap with either $|0\rangle$ or $|\mathbb{Z}_2\rangle$ states. We supplement our numerical results with those from an analytic Floquet Hamiltonian computed using Floquet perturbation theory which allows us to provide qualitative analytical explanations of the above-mentioned numerical results.

I. INTRODUCTION

The physics of nonequilibrium quantum systems has been studied extensively in recent years [1–8]. The theoretical studies in the field have been boosted by possibility of experimental realization using ultracold-atom platforms [9–13]. Out of the several possible drive protocols that could be used to take a quantum system out of equilibrium, periodic drives have attracted a lot of recent attention [6–8]. For such protocols characterized by a time period T, the unitary evolution operator $U(t, 0)$ governs the dynamics of the system. At times $t = nT$, (where $n \in Z$) U can be written in terms of the Floquet Hamiltonian H_F: $U(nT, 0) = \exp[-iH_F nT/\hbar]$, where $\hbar$ is Planck's constant. Thus, the stroboscopic dynamics of the system is completely governed by its Floquet Hamiltonian [8].

The interest in such drive protocols stems from several interesting physical phenomena which occur in periodically driven systems. These include drive-induced nontrivial topology [14–16], dynamical localization [17–20], dynamical phase transitions [21–23], realization of time crystals [24–26], dynamical freezing [27–32], and the possibility of tuning ergodicity property of the driven system [33]. More recently, some of these properties have also been investigated in the context of quasiperiodically [34–36] and aperiodically [36] driven systems.

A central paradigm for understanding the behavior of nonintegrable many-body systems described by local Hamiltonians that are driven out of equilibrium comes from the eigenstate thermalization hypothesis (ETH) [37–40]. ETH

postulates that the reduced density matrix of any eigenstate with finite-energy density is thermal in the thermodynamic limit, the corresponding temperature being determined by its energy density. ETH has also proved successful in explaining properties of nonintegrable systems in the presence of a periodic drive; here eigenstates of the Floquet Hamiltonian play a similar role [40].

The violation of ETH in many-body systems can occur via several routes [32,33,41–60]. For example, ETH does not hold for integrable models where the presence of an extensive number of additional conserved quantities makes the system nonergodic. Moreover, a loss of ergodicity and hence violation of ETH may also happen due to strong disorder when a system enters a many-body localized (MBL) phase [41–45]. Such violation may also occur due to Hilbert space fragmentation where the system Hilbert space organizes into dynamically disconnected sectors [57–60].

Another weaker version of ETH violation has also been found in Rydberg atom systems [32,33,46–49,52]. Experiments on such systems showed coherent long-lived oscillation of density of Rydberg excitations during evolution starting from a Neel state with one Rydberg excitation at every even ($|\mathbb{Z}_2\rangle = |\ldots 1_{2j}, 0_{2j+1}, 1_{2j+2}, \ldots\rangle$) or odd ($|\bar{\mathbb{Z}}_2\rangle = |\ldots 1_{2j-1}, 0_{2j}, 1_{2j+1}, \ldots\rangle$) site; in contrast, ETH predicted thermalization occurred when the dynamics started from the Rydberg vacuum state ($|0\rangle = |..0_j, 0_{j+1}, \rangle$) [13]. The reason for such ETH violating oscillations was traced to the existence of a special class of eigenstates called quantum scars [32,33,46–56]. These are many-body eigenstates with

finite-energy density but anomalously low-entanglement entropy. Consequently, dynamics starting from an initial state which has large overlap with them does not show thermalization. The role of such states in periodically driven Rydberg chain has also been analyzed [32,33]; it was shown that their presence may lead to the possibility of drive-frequency-induced tuning ergodicity property of these chains [33], presence of subthermal steady states, and the phenomenon of dynamical freezing [32]. These properties do not have any analog for scar-induced dynamics following a quench.

More recently, there have been several studies on the possible role of confinement in condensed matter systems. The concept of confinement in one-dimensional (1D) quantum electrodynamics is well known; it was shown that such systems are characterized by a parameter θ which is related to the background electric field. For $\theta = \pi$, the system is deconfined and charge excitations can propagate; for other values of θ, these excitations are confined [61,62]. Such ideas have also been applied to the simulation of lattice gauge theories (LGTs) using ultracold-atom platforms [63–68], Ising-type chains [69], and Rydberg chains with staggered detuning described by the Hamiltonian [46,52,70–72]

$$H_{\text{Ryd}} = -w \sum_j \tilde{\sigma}_j^x - \frac{1}{2} \sum_j [\lambda + \Delta(-1)^j] \sigma_j^z. \qquad (1)$$

Here $\Delta > 0$ and λ denote the amplitude of staggered and uniform detuning, respectively, $w > 0$ is the coupling strength between ground and excited states of the Rydberg atoms, $\sigma_j^z = 2\hat{n}_j - 1$ is related to the number operator $\hat{n}_j$ for a Rydberg excitations on site j. The Hamiltonian given by Eq. (1) is to be supplemented by a constraint that two adjacent sites can not both have Rydberg excitations. Thus, the model has a Rydberg blockade radius of one lattice site. This constraint is implemented using the projected spin operators $\tilde{\sigma}_j^x = P_{j-1}\sigma_j^x P_{j+1}$, where $P_{j-1} = (1 - \sigma_j^z)/2$. The dynamics of such Rydberg chains was studied in context of quench protocols in Refs. [52,70]. It was observed that the presence of the confinement terms leads to slow dynamics of the Rydberg atoms. However, periodic drive protocols for chains with such confinement terms have not been studied so far.

In this work, we study a periodically driven Rydberg chain with a staggered detuning term. Here we consider the uniform detuning parameter λ to be a periodic function of time given by

$$\lambda(t) = \lambda_0, \quad t \leqslant T/2$$
$$= -\lambda_0, \quad t > T/2 \qquad (2)$$

where $T = 2\pi/\omega_D$, ω_D is the drive frequency, and we focus in the regime of large drive amplitude: $\lambda_0 \gg \Delta, w$. In the rest of this work we focus on the dynamics of the density-density correlation function $O_{j2} = \langle \hat{n}_j \hat{n}_{j+2} \rangle$ of these driven Rydberg atoms and the half-chain entanglement entropy $S_{L/2}$ of their Floquet eigenstates. We use ED to study the properties of $S_{L/2}$ and O_{j2} numerically. We supplement our numerical finding by comparing them with those obtained from an analytic, albeit perturbative, Floquet Hamiltonian derived using Floquet perturbation theory (FPT) [8]. We note that such a perturbation theory does not use $1/\omega_D$ as an expansion parameter and is therefore distinct from high-frequency expansions carried

out in the literature [8,73,74]. In contrast, it uses inverse of the drive amplitude as the perturbation parameter and can therefore address the dynamics in the intermediate frequency regime [32,33]. The main results that we obtain from such a study are as follows.

First, we show, via study of $S_{L/2}$, the presence of clustering of Floquet eigenstates in these systems for strong staggered detuning and at intermediate frequencies leading to violation of ETH. These clusters can be classified into two categories. The first type, dubbed as primary clusters, is a result of near-integrable nature of the system for large staggered detuning. The second type of clusters occurs within each primary cluster at a much smaller quasienergy scale. We show, via explicit calculation detailed in Appendix B, that these secondary clusters result from an emergent conservation law found earlier in nondriven Rydberg chains [52].

Second, we also show that the secondary clustering is destroyed, leading to ergodicity restoration within each primary cluster, at commensurate drive frequencies $\hbar\omega_D = n\Delta$, where n is an integer; this allows drive-induced tuning of ergodicity property of the Floquet eigenstates within each primary cluster. To the best of our knowledge, such drive-induced ergodicity restoration has not been so far reported for Rydberg chains with staggered detuning.

Third, we show that for almost all intermediate drive frequencies, O_{22} does not reach its ETH predicted steady-state value; this phenomenon is seen for $|\mathbb{Z}_2\rangle$, $|0\rangle$, and the $|\bar{\mathbb{Z}}_2\rangle$ initial states. For dynamics starting from $|\mathbb{Z}_2\rangle$ and $|0\rangle$ initial states, we find specific drive frequencies for which the system is dynamically frozen; O_{22} remains pinned to its initial values at these frequencies. Around these freezing frequencies, O_{22} displays oscillatory behavior around its initial values with perfect revivals. We provide a semianalytic explanation of the properties of these oscillations in Appendix C.

Fourth, in contrast to the above cases, for the $|\bar{\mathbb{Z}}_2\rangle$ initial state, O_{22} remains frozen over a range of frequencies leading to a dynamically frozen phase. We provide a qualitative explanation for this unusual phenomenon which does not have a counterpart in periodic dynamics of Rydberg chains without uniform detuning [32,33]; our analysis, detailed in Appendix C, also shows that for odd j, O_{j2} will have a frozen phase for dynamics starting from $|\mathbb{Z}_2\rangle$. This dichotomy is a direct consequence of the Z_2 (between even and odd sites) symmetry breaking due to the presence of the staggered detuning.

Fifth, we study the fate of the quantum many-body scars in the Floquet eigenspectrum as a function of the staggered detuning. For small Δ, these scars have almost equal overlap with both the Neel states and we find that scars with $E_F < 0$ ($E_F > 0$) have stronger overlap with $|\mathbb{Z}_2\rangle$ ($|\bar{\mathbb{Z}}_2\rangle$). For large enough Δ, we demonstrate the existence of mid-spectrum scars ($E_F \simeq 0$) which do not show significant overlap with either of the Neel states. Instead, we find that they constitute a separate type of scar states exhibiting high overlap either with classical Fock states with broken Z_4 symmetry ($|\mathbb{Z}_4\rangle$) or with states having single Rydberg excitation ($|1\rangle$). These scar states result in long-time coherent oscillations for dynamics starting from $|\mathbb{Z}_4\rangle$ or $|1\rangle$ initial states and are therefore qualitatively different from their counterparts in the PXP model [47]. To the best of our knowledge, such quantum scars have not been reported earlier in the literature. We also present a

computation of the scars at small and intermediate Δ using a FSA formalism (where FSA stands for forward scattering approximation) in Appendix D.

The plan of the rest of the paper is as follows. In Sec. II, we obtain the analytic Floquet Hamiltonian using FPT. This is followed by Sec. III where we study the structure of the Floquet eigenspectrum for strong staggered detuning and discuss the resultant clustering. Next, in Sec. IV, we analyze the dynamical freezing of O_{22} and its dynamics near the freezing points. This is followed by Sec. V where we discuss the change in properties of the quantum many-body scars in the Floquet eigenspectra as Δ is tuned from small to large values. Finally, we summarize our main results and conclude in Sec. VI. Several technical details of our work are discussed in the Appendixes as mentioned earlier in this section.

II. DERIVATION OF THE FLOQUET HAMILTONIAN

In this section, we derive an analytic Floquet Hamiltonian for the driven Rydberg atoms described by Eq. (1) in the presence of the drive protocol given by Eq. (2). To this end, we shall focus on the limit $\lambda_0 \gg \Delta, w$; however, no restriction is placed on the relative magnitude of Δ and w. For the rest of this section, we shall set $\hbar = 1$.

In what follows, we shall use FPT to obtain the Floquet Hamiltonian [8,9,32]. Since $\lambda_0 \gg \Delta, w$, we treat the uniform detuning term exactly and rewrite Eq. (1) as $H = H_0(t) +$

$H_1 + H_2$ where

$$H_0(t) = -\frac{1}{2}\lambda(t)\sum_j \sigma_j^z,$$

$$H_1 = -\frac{1}{2}\sum_j \Delta(-1)^j \sigma_j^z, \quad H_2 = -w\sum_j \tilde{\sigma}_j^x. \quad (3)$$

We shall treat H_1 and H_2 perturbatively. This leads to the evolution operator

$$U_0(t, 0) = T_t\{e^{-i\int_0^t H_0(t')dt'}\}$$
$$= e^{i\lambda_0 t \sum_j \sigma_j^z/2}, \quad t \leqslant T/2$$
$$= e^{i\lambda_0(T-t)\sum_j \sigma_j^z/2}, \quad t \geqslant T/2. \quad (4)$$

We note that $U_0(T, 0) = I$ which leads to $H_F^{(0)} = 0$. Also, for subsequent computation, we define the states $|m\rangle$ as eigenstates of H_0 that have m up spins and $L - m$ down spins. Such states need to obey the constraint imposed by the model; thus, $m_{\max} = L/2$ is the maximum number of up spins.

Next, we consider the first-order correction to the Floquet Hamiltonian given, within FPT, by

$$U_1(T, 0) = -i\int_0^T dt_1 U_0^\dagger(t_1, 0)(H_1 + H_2)U_0(t_1, 0). \quad (5)$$

To evaluate U_1, we note that H_1 commutes with U_0. Moreover, the contribution from H_2 has already been obtained in Refs. [32,33]. From these we find

$$\langle m|U_1(T, 0)|n\rangle = iT\sum_m \left(\sum_j \frac{\Delta}{2}(-1)^j\langle m|\sigma_j^z|m\rangle|m\rangle\langle m|\delta_{mn} + \sum_{s_j=\pm1} \frac{4iw}{\lambda_0 T}\sin\frac{\lambda_0 T}{4}e^{i\lambda_0 T s_j}|m\rangle\langle m + s_j|\delta_{n,m+s_j}\right). \quad (6)$$

Using Eq. (6), one obtains the first-order Floquet Hamiltonian, given by $H_F^{(1)}(\Delta, w_r) \equiv H_F^{(1)} = iU_1(T, 0)/T$, to be

$$H_F^{(1)}(\Delta, w_r) = -\Delta Z_\pi - w_r\sum_j(\cos\gamma\,\tilde{\sigma}_x + \sin\gamma\,\tilde{\sigma}_y),$$

$$Z_\pi = \frac{1}{2}\sum_j(-1)^j\sigma_j^z, \quad w_r = \frac{w\sin\gamma}{\gamma}, \quad (7)$$

where $\gamma = \lambda_0 T/4$. We note that the second term in $H_F^{(1)}$, obtained in Refs. [32,33], vanishes at $\gamma = n\pi$ (or $\lambda_0 = 2n\omega_D$) for nonzero integer n; thus, at these points, we expect the effect of the staggered detuning term (H_1) to be particularly strong.

The next higher-order correction to the Floquet Hamiltonian comes from $O(w^3)$ terms in the Floquet Hamiltonian. The derivation of these corrections can be found in Appendix A. The main effects of these terms are to renormalize the Floquet Hamiltonian obtained within first order and to provide three-spin interaction terms. As shown in Appendix A, the final Floquet Hamiltonian is given by

$$H_F = H_F^{(1)}(\Delta_r, w_r) + H_{F3}^{(2)} + H_F^{(3)} + \cdots,$$

$$\Delta_r = \Delta\left[1 - \frac{w^2 T^2}{8\gamma^3}\left(\frac{1}{2}\sin 2\gamma - \gamma\cos 2\gamma\right) + \cdots\right], \quad (8)$$

where the ellipses indicate higher-order contribution to the Floquet Hamiltonian and Δ_r denote the renormalized amplitude of the staggered term obtained using Eq. (A9) in Appendix A. The other terms, $H_F^{(2)}$ and $H_F^{(3)}$, are given in Eqs. (A6) and (A10), respectively; their derivation has been sketched in Appendix A. In what follows, we shall use Eq. (8) to analyze our numerical results; in most cases, we find that the effect of the third-order terms $H_F^{(2)}$ and $H_F^{(3)}$ obtained in Appendix A are small and $H_F \simeq H_F^{(1)}(\Delta_r, w_r)$ for our purpose.

III. STRONG STAGGERED DETUNING

In this and the next two sections, we present the main results of our study obtained by exact numerics and compare them to those obtained from the analytic Floquet Hamiltonian derived in Sec. II. In the present section, we shall restrict ourselves to the strong staggered detuning limit ($\Delta \geqslant w$), while other parameter regimes will be explored in Secs. IV and V.

The exact numerical results that we present are obtained using exact diagonalization (ED) on finite-sized chain as follows [32,33]. We first numerically diagonalize $H(\pm\lambda_0) = H_0(\pm\lambda_0) + H_1 + H_2$ [Eq. (3)] to obtain their energy
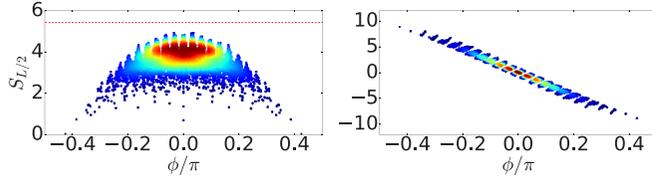
FIG. 1. Left: Plot of $S_{L/2}$ as a function of $\phi = E_F T/\hbar$ for $\omega_D = 100w/\hbar$. The red dotted line is the ETH predicted Page value of $S_{L/2}$. Right panel: Plot of $\langle Z_\pi \rangle$ for Floquet eigenstates as a function of ϕ for same ω_D. For both plots $L = 24$, $\Delta/w = 1.2$, and $\lambda/w = 15$. All energies are scaled in units of w and frequencies in units of $w/\hbar$. The color scheme indicates higher density of states for warmer colors. See text for details.

eigenvalues $\epsilon_a^\pm$ and eigenvectors $|\xi_a^\pm\rangle$. The evolution operator for the square-pulse protocol [Eq. (2)] can then be written as

$$U(T,0) = e^{-iH_F(-\lambda_0)T/(2\hbar)} e^{-iH_F(\lambda_0)T/(2\hbar)}$$
$$= \sum_{a,b} c_{ab}^{-+} e^{-i(\epsilon_a^- + \epsilon_b^+)T/(2\hbar)} |\xi_a^-\rangle \langle \xi_b^+|, \qquad (9)$$

where $c_{ab}^{-+} = \langle \xi_a^- | \xi_b^+ \rangle$. We then numerically diagonalize the unitary matrix U to obtain its eigenvalues $\lambda_n = \exp[-iE_n^F T/\hbar]$ and eigenvectors $|\chi_n\rangle$. The exact Floquet Hamiltonian of the system can then be obtained as

$$H_F = \sum_n E_n^F |\chi_n\rangle \langle \chi_n|. \qquad (10)$$

In what follows, we shall use Eq. (10) for numerical computation of the Floquet Hamiltonian. Most of the numerical results in the rest of this section, unless explicitly mentioned otherwise, correspond to $\lambda = 15$ and $w = 1$.

A. Clustering of Floquet eigenstates

In this section, we discuss the structure of the Hilbert space spanned by Floquet eigenstates of the driven staggered Rydberg chain. To this end, we plot the half-chain entanglement entropy $S_{L/2}$ of these eigenstates as a function of their quasienergy E_F. The details of the numerical procedure used for this computation are same as that charted in Ref. [33]. The first step involves writing the density matrix $\rho_n = |\chi_n\rangle \langle \chi_n|$ corresponding to the nth Floquet eigenstate. One then integrates out the contribution to this state from Fock states residing on one half of the chain; such an operation has to be carried out numerically without violating the constraint condition as detailed in Ref. [33]. This leads to the reduced density matrix ρ_n^{red}. The von Neumann entanglement entropy is then computed from ρ_n^{red} following the standard prescription: $S_{L/2}^{(n)} \equiv S_{L/2} = -\text{Tr}[\rho_n^{\text{red}} \ln \rho_n^{\text{red}}]$. For finite-sized periodically driven systems, the prediction of ETH for $S_{L/2}$ is given by the Page formula: $S_{L/2}^{\text{Page}} = \ln \text{HSD} - 1/2$, where HSD denotes Hilbert space dimension of the half-chain with open boundary condition, and HSD $= 377$ for $L = 24$.

The result of such a computation is shown in Figs. 1 and 2 for $\Delta = 1.2w$. From Fig. 1, we find that the Hilbert space is ergodic at high drive frequencies for which $w_r \simeq w$. In contrast, as seen from Fig. 2, it fragments into several clusters
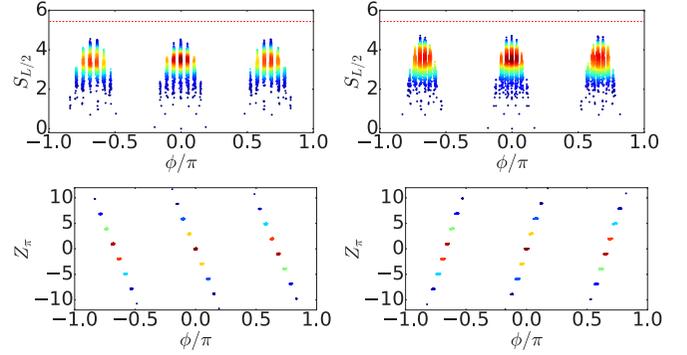
FIG. 2. Top left panel: Plot of $S_{L/2}$ as a function of Floquet quasienergies $\phi = E_F T/\hbar$ for $\omega_D = 3.5w/\hbar$. Top right panel: A similar plot for $\omega_D = 3.65w/\hbar$. Bottom left panel: Plot of $\langle Z_\pi \rangle$ for Floquet eigenstates as a function of ϕ for $\omega_D = 3.5w/\hbar$. Bottom right panel: Similar plot as the bottom left panel but for $\omega_D = 3.65w/\hbar$. For all plots $L = 24$, $\Delta = 1.2w$, and $\lambda = 15w$. All energies are scaled in units of w and frequencies in units of $w/\hbar$. The color scheme is same as in Fig. 1 and the red dotted lines in the top panel indicate ETH predicted Page value of $S_{L/2}$. See text for details.

at intermediate ω_D. We dub these clusters as primary clusters. Their origin can be straightforwardly understood as follows.

We note that the leading terms in the Floquet Hamiltonian are given by H_{F1}. For $\lambda T/\hbar \lesssim 1$ ($\omega_D = 100w/\hbar$), when $w_r \sim w$, the amplitude of the staggered and the PXP terms in H_{F1} are comparable and their eigenstates span the entire Hilbert space as expected for a nonintegrable model. This behavior is shown in the left panel of Fig. 1 and is further highlighted by plotting the expectation value of Z_π [Eq. (7)] for these states, as shown in the right panel of Fig. 1. We find that the quasienergy difference between the states with different $\langle Z_\pi \rangle$ are $O(w)$; hence, $w_r \sim w$ can hybridize states with different $\langle Z_\pi \rangle$ leading to ergodicity.

In contrast, for $\omega_D \sim 3.5w/\hbar$ and $3.65w/\hbar$, $w_r \ll w, \Delta$. In this limit, the model is near integrable and the eigenstates cluster into groups as shown in the top panels of Fig. 2. Each of these groups have states with definite values $\langle Z_\pi \rangle$ and dimensionless quasienergy

$$\phi = \frac{E_F T}{\hbar} \simeq -\frac{\Delta_r T}{\hbar} \langle Z_\pi \rangle \qquad (11)$$

as shown in the bottom panels of Fig. 2. It is crucial to note here that ϕ is 2π periodic; thus, Floquet eigenstates with quasienergy outside the range $-\pi \leqslant \phi \leqslant \pi$ have to be folded back, using this periodicity, to the first Floquet-Brillouin zone. The primary clustering is therefore a consequence of near integrability of H_F for small w_r/Δ_r.

The eigenstates within the central primary cluster seen in the top panel of Fig. 2 have $\langle Z_\pi \rangle = \pm 3n$ while the other clusters have $\langle Z_\pi \rangle = \pm 3n + 1$ and $\pm 3n + 2$ where n is an integer. The number of such primary clusters can be deduced from the fact that for the parameter regime of these plots $\Delta_r/(\hbar \omega_D) \sim \frac{1}{3}$. Importantly, Δ_r is still incommensurate to the drive frequency by a small amount (the exact commensuration occurs at $\Delta_r = \hbar \omega_D/3 \sim 1.2w$) so that states within the same cluster are nondegenerate. This incommensuration can
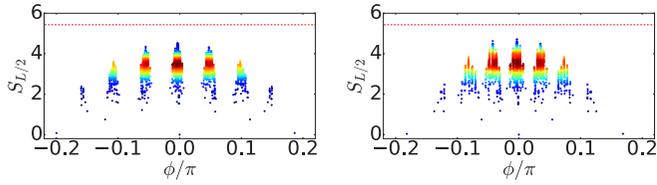
FIG. 3. Left panel: Plot of $S_{L/2}$ as a function of Floquet quasienergies $\phi = E_F T/\hbar$ within the central primary cluster for $\omega_D = 3.5w/\hbar$. Right panel: A similar plot for $\omega_D = 3.65w/\hbar$. For all plots $L = 24$, $\Delta = 1.2w$, and $\lambda = 15w$. All energies are scaled in units of w and frequencies in units of $w/\hbar$. The color scheme is same as in Fig. 1 and the red dotted lines in the top panel indicate ETH predicted Page value of $S_{L/2}$. See text for details.

be parametrized by a dimensionless ratio given by

$$x = \frac{\hbar\omega_D}{\Delta_r} - 3. \qquad (12)$$

For $\Delta = 1.2$, $x \simeq -0.0834$ for $\omega_D = 3.5w/\hbar$ and 0.04167 for $\omega_D = 3.65w/\hbar$. The primary clusters, for $w_r \ll \Delta_r$, are separated with quasienergies ϕ_1 while the states within each cluster are separated by smaller quasienergy scale ϕ_2, where

$$\phi_1 = \delta E_1 T/\hbar \sim 2\pi/(3 + x),$$
$$\phi_2 = \delta E_2 T/\hbar \sim |x| 2\pi/(3 + x). \qquad (13)$$

In the parameter regime of our numerics, where $w_r \ll \delta E_1$, the primary clustering is not destroyed by w_r for finite-sized chains with $L \leqslant 24$.

A closer inspection of the primary clusters reveals that each of them, with definite values of Z_π, exhibit further clustering. The left (right) panel of Fig. 3 shows such clustering for $\omega_D = 3.5 (3.65)w/\hbar$. We dub this phenomenon as secondary clustering. The origin of such secondary clustering can be understood via construction of an effective Floquet Hamiltonian in the regime $w_r \sim \delta E_2 \ll \delta E_1$. The analysis is same as what has been carried out in Ref. [52] and has been detailed in Appendix B. Such a Hamiltonian, given by Eqs. (B4) and (B5), shows that w_r can have significant nonzero matrix elements only between states within each primary cluster. Moreover, as shown in Ref. [52], the presence of a finite w_r does not lead to ergodic structure within each primary cluster. Instead, a perturbative analysis, similar to that carried out in Ref. [52] and detailed in Appendix B, indicates that the secondary clustering occurs due to an emergent conserved quantity [Eq. (B5)]

$$Y = -\sum_j (-1)^j P_{j-1} \sigma_j^z P_{j+1}, \qquad (14)$$

within each Z_π sector. These secondary clusters correspond to groups of states with same values of $\langle Y \rangle$. This can be clearly seen from Fig. 4 where $\langle Y \rangle$ is plotted for eigenstates in each of the primary clusters. We find a definite value of $\langle Y \rangle$ for all Floquet eigenstates both at $\hbar\omega_D = 3.65w$ and $3.5w$ as can be seen from the top and bottom panels of Fig. 4, respectively. We note that the emergence of Y relies on the perturbative parameter $w_r/\delta E_2 \leqslant 1$. Such a perturbation theory will break down for at the exact commensuration point where x, and hence δE_2, vanishes. This leads to loss of secondary clustering. At
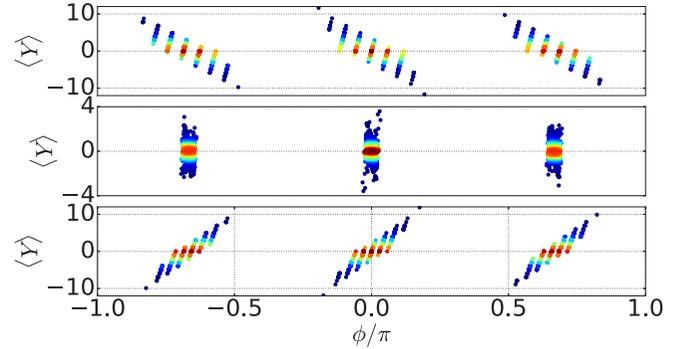
FIG. 4. Plot of $\langle Y \rangle$ for the Floquet eigenstates as a function of $\phi = E_F T/\hbar$ for $\hbar\omega_D = 3.65w$ (top panel), $3.58w$ (middle panel), and $3.5w$ (bottom panel). For all plots $L = 24$, $\lambda/w = 15$, and $\Delta/w = 1.2$. All energies are scaled in units of w and frequencies in units of $w/\hbar$. The color scheme is same as in Fig. 1 and the black dashed lines are guide to the eye. See text for details.

these commensuration points, the Floquet eigenstates can not be associated with a definite $\langle Y \rangle$ value as can be seen from the middle panel of Fig. 4. We shall discuss this case in Sec. III B.

B. Ergodicity restoration

In this section, we discuss the behavior of the driven chain when the amplitude of the staggered detuning is commensurate with the drive frequency. To this end, we first note that for $\hbar\omega_D/\Delta_r = n$ where $n \in Z$, one can write

$$U(T, 0) = e^{-iH_F T/\hbar} = e^{-i[H_1' T + (2\pi/n)Z_\pi]/\hbar}. \qquad (15)$$

Thus, for $n = 3$, the Floquet eigenstates can be organized into clusters of states with values of $\langle Z_\pi \rangle = \pm 3n$, $\pm 3n + 1$, and $\pm 3n + 2$. This is seen in the top left panel of Fig. 5. We also note that each of the states in a given primary cluster shall have identical quasienergy at $w_r = 0$ since x, and hence δE_2, vanishes. Thus, in absence of w_r, they form a flat band and the Hilbert space comprises of three such flat bands with $\delta E_1 = 0$ and $\pm\hbar\omega_D/3$ in this limit. The number of such clusters depends on n; this is exhibited in Fig. 6 where the structure of the states with $n = 2$ and 4 primary clusters is shown.

In the presence of a nonzero w_r, within each cluster, the effective Floquet Hamiltonian is given by H_1'. For small w_r, the primary clustering still exists for finite L since $w_r \ll \Delta$. However, within each primary cluster, $H_F^{\text{eff}} \simeq H_1'$ since $\delta E_2 = 0$. Thus, the effective Floquet Hamiltonian for each primary cluster resembles a renormalized PXP Hamiltonian along with higher-order terms. The states within each primary cluster are therefore expected to have an ergodic structure with no secondary clustering. Moreover, as seen from the right panel of Fig. 5, they possess a continuous range of $\langle Z_\pi \rangle$ values for any finite w_r. This property stems from strong hybridization between states with definite integer values of $\langle Z_\pi \rangle$ in the presence of nonzero w_r. We note that the perturbative analysis derived in Ref. [52] leading to the emergent invariant Y responsible for the secondary clustering becomes invalid here since the perturbative parameter $w_r/\delta E_2 \to \infty$ at the commensuration point. This expectation is validated from exact numerics as seen from the central panel of Fig. 5 where the ergodic structure for states within the central primary
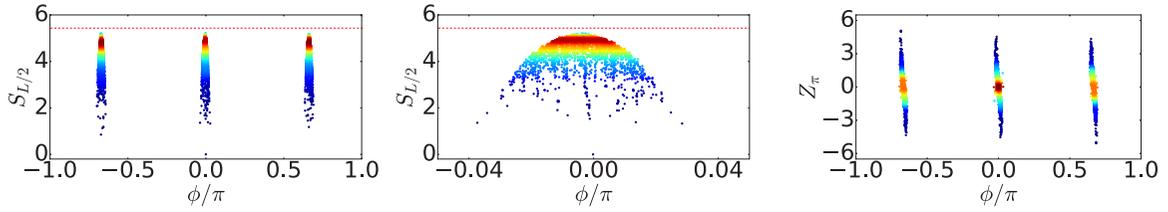
FIG. 5. Left panel: Plot of $S_{L/2}$ as a function of $\phi = E_F T/\hbar$ for $\omega_D = 3.58 w/\hbar$. Central panel: A similar plot showing states within the primary cluster around $E_F = 0$. Right panel: Plot of $\langle Z_\pi \rangle$ as a function of ϕ. For all plots $\Delta/w = 1.2$, and $\lambda/w = 15$. All energies are scaled in units of w and frequencies in units of $w/\hbar$. The color scheme is same as in Fig. 1 and the red dotted lines in the left and central panels indicate ETH predicted Page value of $S_{L/2}$. See text for details.

cluster is shown. We note that each of the clusters contain both anomalous states with low $S_{L/2}$ along with thermal states with high $S_{L/2}$. A similar behavior is expected for the $s = \pm 1$ primary clusters.

The consequence of such ergodicity restoration within a primary cluster is also reflected in the steady-state value of O_{22}, O_{22}^{DE}, as shown in Fig. 7. The steady-state value of O_{22}, in terms of the Floquet spectrum, is given by

$$O_{22}^{DE} = \sum_n \left| c_n^{init} \right|^2 \langle n | \hat{n}_2 \hat{n}_4 | n \rangle, \qquad (16)$$

where $c_n^{init} = \langle n | \psi_0 \rangle$ and $|\psi_0\rangle \equiv |\bar{\mathbb{Z}}_2\rangle$, $|\mathbb{Z}_2\rangle$, or $|0\rangle$ is the overlap of the Floquet eigenstates $|n\rangle$ with the initial state. We find that O_{22}^{DE} exhibits a sharp dip at the commensuration point when the dynamics starts from $|\mathbb{Z}_2\rangle$; in contrast, it exhibits a smaller peak for $|\bar{\mathbb{Z}}_2\rangle$ initial state. In both cases, its value approaches close to that predicted by ETH: $O_{22}^{ETH} \sim 0.11$. This is clearly a consequence of restoration of ergodicity within a primary cluster. As one varies the frequency away from the commensuration point, O_{22}^{DE} deviates sharply from its ETH predicted value approximately around $w_r \simeq \delta E_2$. The sharpness of such deviation is a consequence of small $w_r \simeq 0.045$ at $\lambda = 15w$ and $\hbar \omega_D = 3.58w$; this can be controlled by varying λ which tunes w_r for a fixed ω_D. The stroboscopic evolution of O_{22} at these ergodicity restoring points does not

display coherent oscillations as can be seen from the inset of Fig. 7; instead, it displays a slow approach to the thermal steady state.

IV. DYNAMICAL FREEZING

In this section, we present our results on the density-density correlation function $O_{j2} = \langle \hat{n}_j \hat{n}_{j+2} \rangle$ with focus on dynamical freezing of these correlations at specific drive frequencies and their oscillations near these freezing frequencies. For all numerical results in this section, we shall choose $j = 2$.

We begin with a study of the behavior of O_{22}^{DE} as a function of Δ/w as shown in Fig. 8. The plot shows its behavior for the initial Neel ($|\mathbb{Z}_2\rangle$ and $|\bar{\mathbb{Z}}_2\rangle$) and vacuum ($|0\rangle$) states. It indicates strong deviation from the ETH predicted value $O_{22}^{ETH} \simeq 0.11$ at intermediate drive frequencies. For the $|0\rangle$ initial state, O_{22}^{DE} reaches its ETH predicted value at high drive frequencies where $w_r \sim w \simeq \Delta$ as expected; in contrast, for the $|\mathbb{Z}_2\rangle$ initial state, O_{22}^{DE} reaches a superthermal value. The latter behavior can be attributed to the presence of scar states in the Floquet spectra with large overlap with the $|\mathbb{Z}_2\rangle$ states
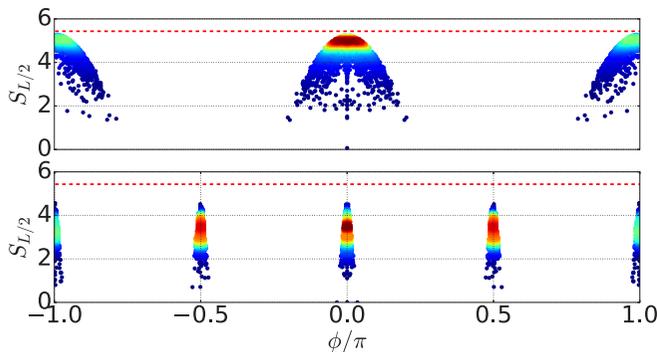
FIG. 6. Top panel: Plot of $S_{L/2}$ as a function of Floquet quasienergies $\phi = E_F T/\hbar$ for $\Delta/w = 1.8$ showing two primary clusters. Bottom panel: A similar plot for $\Delta/w = 0.9$ showing four primary clusters. For both plots $\hbar \omega_D/w = 3.6w$ and $\lambda/w = 15$. All energies are scaled in units of w and frequencies in units of $w/\hbar$. The color scheme is same as in Fig. 1 and the red dotted lines indicate ETH predicted Page value of $S_{L/2}$. The black dashed lines are guide to the eye. See text for details.
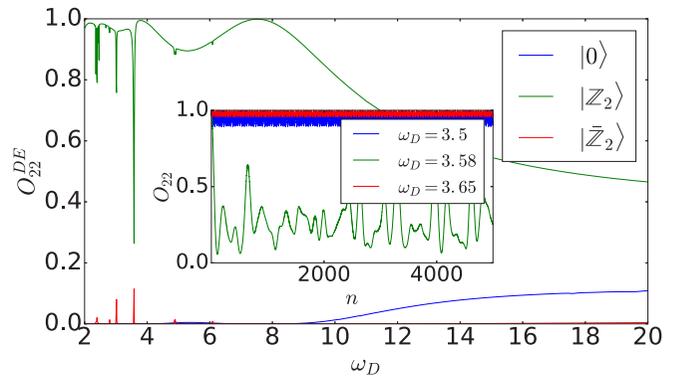
FIG. 7. Plot of the steady-state value of $O_{22} \equiv O_{22}^{DE}$ as a function ω_D for $\Delta/w = 1.2$ showing restoration of ergodicity at special frequencies. Such restoration is characterized by sharp dips in the O_{22}^{DE} value approaching the ETH prediction $O_{22}^{ETH} \sim 0.11$. The inset shows the dynamics of O_{22} starting from a $|\mathbb{Z}_2\rangle$ state as a function of n for commensurate ($\hbar \omega_D/w = 3.58$) and slightly incommensurate ($\hbar \omega_D/w = 3.65$ and $\hbar \omega_D/w = 3.5$) drive frequencies. The coherent oscillations of O_{22} (shown above for $\hbar \omega_d/w = 3.5$ and 3.65) seen at incommensurate frequencies are replaced by a slower approach to the steady state at exactly commensurate drive frequency ($\hbar \omega_D/w = 3.58$). All energies (frequencies) are scaled in units of $w(w/\hbar)$. See text for details.
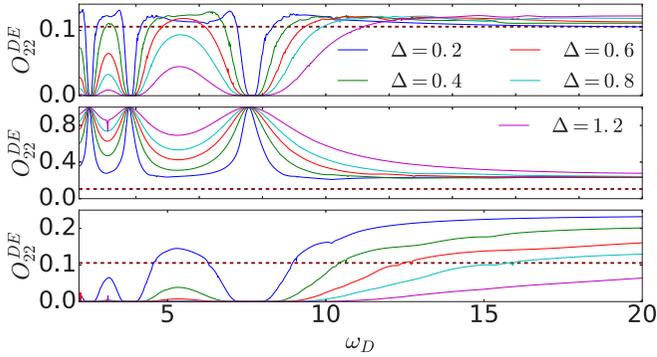
FIG. 8. Plot of the steady-state value of $O_{22} \equiv O_{22}^{DE}$ as a function of ω_D starting from the $|0\rangle$ (top panel), $|\mathbb{Z}_2\rangle$ (middle panel), and $|\bar{\mathbb{Z}}_2\rangle$ (bottom panel) states for several representative values of Δ/w as shown. The maroon dashed lines indicate the ETH predicted value $O_{22}^{\rm ETH}$. For all plots $\lambda/w = 15$. All energies are scaled in units of w and frequencies in units of $w/\hbar$. See text for details.

[32,33]; we shall discuss these states in Sec. V. For either of these initial states, O_{22}^{DE}, in the high-frequency limit, is almost independent of Δ as long as $w \geqslant \Delta$. In contrast, it depends strongly on Δ for $\hbar\omega_D \gg w$ and can take either superthermal or subthermal values for $|\bar{\mathbb{Z}}_2\rangle$ initial state; this constitutes a stronger violation of ETH which can not be explained by presence of scars alone.

To see why this is the case, we note that $\Delta/w \ll 1$, the value of O_{22}^{DE} is expected to be identical irrespective of whether the starting state is $|\mathbb{Z}_2\rangle$ or $|\bar{\mathbb{Z}}_2\rangle$. This situation is highlighted in the left panels of Fig. 9. The top left panel shows the expectation value $O_{22}^{(m)} = \langle m|\hat{n}_2\hat{n}_4|m\rangle$ corresponding to the Floquet eigenstate $|m\rangle$ as a function of their dimensionless quasienergy $\phi = E_F^{(m)}T/\hbar$. The bottom panel shows the overlap of the eigenstates $|m\rangle$ with the initial states. For small $\Delta/w = 0.2$, we find that the largest value of $O_{22}^{(m)}$ occurs for eigenstates $|m\rangle$ which lie close to the middle of
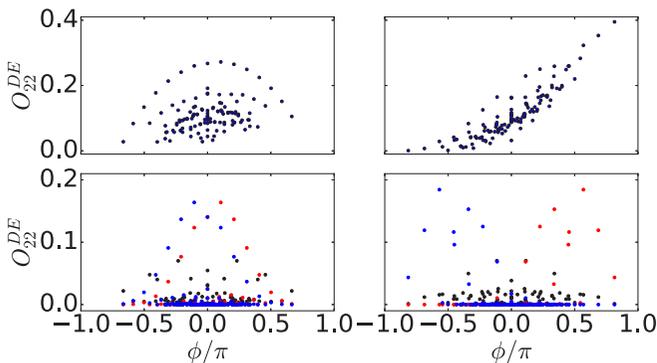
FIG. 9. Top left panel: Plot of $O_{22}^{(m)} = \langle m|\hat{n}_2\hat{n}_4|m\rangle \equiv O_{22}$ corresponding to Floquet eigenstates $|m\rangle$ as a function of their quasienergy $\phi = E_F^{(m)}T/\hbar$ for $\Delta/w = 0.1$. Bottom left panel: Overlap of these eigenstates with $|\mathbb{Z}_2\rangle$ (red dots), $|\bar{\mathbb{Z}}_2\rangle$ (blue dots), and $|0\rangle$ (black dots). Right panels: Same as the corresponding left panels but for $\Delta/w = 1.2$. All left panel plots have same Y axes range as their right panel counterparts. All plots correspond to $L = 14$, $\lambda/w = 15$, and $\hbar\omega_D/w = 6.9$. All energies are scaled in units of w and frequencies in units of $w/\hbar$. See text for details.

the Floquet spectrum ($E_F \simeq 0$). Furthermore, near the middle of the Floquet spectrum, some of these states have significant overlap with $|\mathbb{Z}_2\rangle$ while others have large overlap with $|\bar{\mathbb{Z}}_2\rangle$ as can be seen the left bottom panel of Fig. 9. From Eq. (16), we find that this ensures that $O_{22}^{\rm DE}$ would be almost identical irrespective of whether the dynamics starts from $|\mathbb{Z}_2\rangle$ or $|\bar{\mathbb{Z}}_2\rangle$ initial states; in fact, they have exactly identical values at $\Delta = 0$.

This situation drastically changes at large Δ, where all the Floquet eigenstates with large values of $O_{22}^{(m)}$ have quasienergy $E_F > 0$ as shown in the top right panel of Fig. 9. Moreover, these eigenstates only have large overlap with $|\mathbb{Z}_2\rangle$. Consequently, the value of $O_{22}^{\rm DE}$ does not change appreciably for dynamics starting from $|\mathbb{Z}_2\rangle$ as Δ is increased; however, its value reduces drastically if the initial state is $|\bar{\mathbb{Z}}_2\rangle$. Thus, with increasing Δ, $O_{22}^{\rm DE}$ drops rapidly to subthermal values and approaches zero for the $|\bar{\mathbb{Z}}_2\rangle$ initial state; this leads to qualitatively different Δ dependence of $O_{22}^{\rm DE}$.

In addition, the top and the middle panel plots of Fig. 8 indicate the presence of dynamical freezing at special values of the drive frequencies $\omega_D \simeq \lambda/(2n_0\hbar)$ (where $n_0 \in Z$) for which $w_r \simeq 0$. At these values, the initial states $|0\rangle$, $|\mathbb{Z}_2\rangle$, and $|\bar{\mathbb{Z}}_2\rangle$ become approximate eigenstates of the Floquet Hamiltonian leading to freezing. The neighborhood of these freezing frequencies is marked by strong deviation from the ETH predicted value of O_{22} as shown in the top and middle panels of Fig. 8; this deviation increases with increasing Δ. As discussed in details in Appendix C, O_{22} displays steady oscillations around these points with an amplitude which decreases with Δ and frequency given by $\Delta/\hbar$. In contrast, for $|\bar{\mathbb{Z}}_2\rangle$ initial state and for $\Delta > w$, the freezing extends over a range of frequencies, as seen in the bottom panel of Fig. 8. An explanation of this behavior is also presented in Appendix C. We note here that this behavior stems from the presence of staggered detuning which differentiates between odd and even sites of the chain as explained in details in Appendix C.

V. CROSSOVER FROM WEAK TO STRONG STAGGERED DETUNING

In this section, we shall study the behavior of the quasienergy eigenstates as $\delta E_2/w_r$ is gradually increased. We note at the outset that this behavior can be reproduced by studying the properties of eigenstates of

$$H_m = -\Delta' Z_\pi - \sum_j \tilde{\sigma}_j^x \qquad (17)$$

such that $\Delta' \equiv 2\delta E_2/w_r$. This is due to the fact that a variation of ω_D in $H_F^{(1)}$ can take us close to both the commensuration point where $\delta E_2 \simeq 0$ (for example, for $\Delta \simeq 1.2$ and $\hbar\omega_d \simeq 3.6$) and the dynamical freezing point where $w_r \simeq 0$ (for example, around $\lambda T/\hbar = 4\pi$). We therefore expect this analysis to reveal the nature of the crossover between Hilbert space structure having quantum scars ($\Delta' = 0$) to that having clustering ($\Delta' \gg 1$).

We begin by plotting the entanglement entropy of the eigenstates of H_m as a function of dimensionless energy E for four representative values of Δ' in Fig. 10. The top left panel of Fig. 10 shows the existence of quantum scars for small $\Delta' \ll 1$. These scars which occur close to the
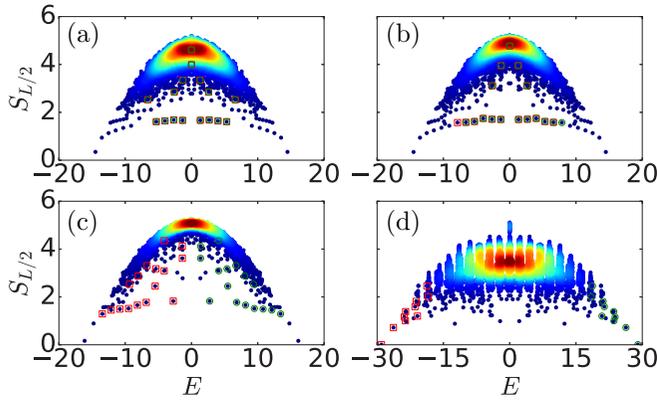
FIG. 10. Plot of the half-chain entanglement $S_{L/2}$ of the eigenstates of H_m as a function of energy E for (a) $\Delta' = 0.005$, (b) 0.05, (c) 0.5, and (d) 2. The green and the red circles indicate states with high overlap with $|\bar{\mathbb{Z}}_2\rangle$ and $|\mathbb{Z}_2\rangle$, respectively. All plots have same Y axes range and correspond to $L = 24$. See text for details.

FIG. 12. Left panel: Plot of $S_{L/2}$ for eigenstates of H_m showing the scar states having large overlap with $|0\rangle$ (black square), $|1\rangle$ (blue square), and $|\mathbb{Z}_4\rangle$ (green square). The red dashed line indicates the ETH predicted Page value of $S_{L/2}$. Right panel: The dynamics of $\langle N_d \rangle$ starting from state $|1\rangle$ (top) and the fidelity $F(t) = |\langle \psi(t)|1\rangle|^2$ (bottom) as a function of time showing scar-induced long-time coherent oscillations. For all plots $L = 24$ and $\Delta' = 5$. See text for details.

commensuration point where $x \ll 1$ have, in accordance with standard expectation, almost equal overlap with $|\mathbb{Z}_2\rangle$ (red circles) and $|\bar{\mathbb{Z}}_2\rangle$ (green circles) states. We find as we increase Δ', the scars with $E_F < 0$ develop higher overlap with $|\mathbb{Z}_2\rangle$ while those with $E_F > 0$ exhibit higher overlap with $|\bar{\mathbb{Z}}_2\rangle$. This asymmetry can be understood from the fact that the presence of a large Δ' pushes the states with high $|\mathbb{Z}_2\rangle$ ($|\bar{\mathbb{Z}}_2\rangle$) overlap to lower (higher) quasienergy. This phenomenon can be easily understood from a FSA analysis as shown in Appendix D. For $\Delta' \gg 1$, there are almost no mid-spectrum states which have high overlap with either $|\mathbb{Z}_2\rangle$ or $|\bar{\mathbb{Z}}_2\rangle$. Remarkably, even in this regime, we find existence of scarlike states as seen from bottom right panel of Fig. 10; these do not show high overlap with either $|\bar{\mathbb{Z}}_2\rangle$ or $|\mathbb{Z}_2\rangle$. This situation is to be contrasted to that in Rydberg chains with uniform detuning where scars disappear at large detuning away from the PXP limit [46,47]. The crossover between these two situations happens between $0.75 \leqslant \Delta' \leqslant 1$ as can be seen from Fig. 11. Thus, at these values of Δ', an almost continuous

FIG. 11. Plot of the half-chain entanglement $S_{L/2}$ of the eigenstates of H_m as a function of energy E for (a) $\Delta' = 0.75$, (b) 1, (c) 1.25, and (d) 1.75. The red circles indicate states with high overlap with $|\mathbb{Z}_2\rangle$. All plots have same Y axes range and correspond to $L = 24$. See text for details.

band of scar states remain although their nature evolves with increasing Δ'.

This structure of scars is preserved at higher values of Δ' where the Hilbert space is strongly clustered. The mid-spectrum states here do not have significant overlap with either $|\mathbb{Z}_2\rangle$ and $|\bar{\mathbb{Z}}_2\rangle$. Instead, as we find numerically and as shown in the left panel of Fig. 12, two of these states have high overlap with $|\mathbb{Z}_4\rangle = |\uparrow, \downarrow, \downarrow, \downarrow, \uparrow, \downarrow, \downarrow, \downarrow \ldots \rangle$ states. Other mid-spectrum scar states have strong overlap either with the single Rydberg excited state $|1\rangle = |\uparrow, \downarrow, \downarrow \ldots \rangle$ or the vacuum state $|0\rangle$ as shown in the left panel of Fig. 12. These mid-spectrum scar states have no analog in their counterparts for small Δ'. Indeed, this can be seen by studying the dynamics of the Rydberg excitation density $\langle N_d \rangle = \langle \sum_j (\sigma_j^z + 1)/2 \rangle$ as a function of time. The fidelity $F_1 = |\langle 1|\psi(t)\rangle|^2$ of these oscillations indicates perfect revivals as can be seen from the bottom right panel of Fig. 12. The presence of such oscillations starting from single spin-up state could not have been due to the $|\mathbb{Z}_2\rangle$ scars. Similar oscillatory coherent dynamics with near perfect fidelity revivals is also seen in this regime for initial states $|0\rangle$ and $|\mathbb{Z}_4\rangle$ as shown in Fig. 13.

The frequencies of these oscillations and the nature of the dynamics starting from the $|\mathbb{Z}_4\rangle$ state can be understood as follows. From the plot of the overlap of the initial state with the Floquet eigenstates, shown in Fig. 14, we find that the overlap of $|\mathbb{Z}_4\rangle$ is maximal with the one of the mid-spectrum scar states. This state has $E_F > 0$ ($E_F < 0$) if the $|\mathbb{Z}_4\rangle$ hosts Rydberg excitations on odd (even) sites; this is due to the presence of a large Δ' in the Hamiltonian which breaks the particle-hole symmetry. The next largest overlap corresponds to two states on both sides of the $|\mathbb{Z}_4\rangle$ states; these have slightly different energies and belong to primary clusters characterized by $Z_\pi = 5$ and 7, respectively. The difference in energy between the Z_4 scar and these two states leads to the main oscillation frequency $\omega \simeq \Delta'/(2\hbar)$; in addition, the small difference in frequencies of these two states leads to a long-time beating phenomenon as can be seen from the right panel Fig. 13. The analysis of the dynamics starting from $|1\rangle$ or $|0\rangle$ reveals a qualitatively similar picture and we do not discuss them in details here.
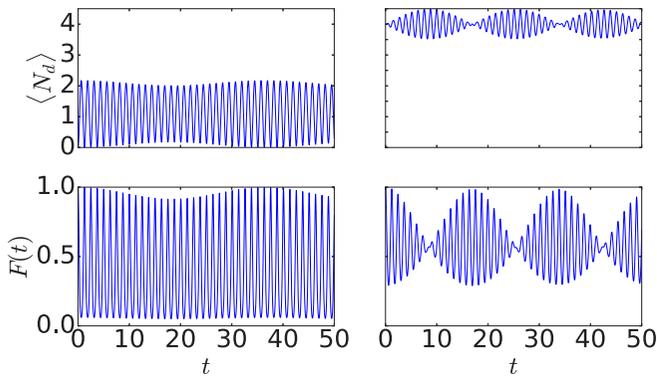
FIG. 13. Left: The dynamics of $\langle N_d \rangle$ (top) starting from the initial state $|0\rangle$ and the fidelity $F(t) = |\langle \psi(t)|0\rangle|^2$ (bottom) as a function of time. Right: Similar plots for the initial $|\mathbb{Z}_4\rangle$ state. All left panel plots have same Y axes range as their right panel counterparts. All plots correspond to $L = 16$ and $\Delta' = 5$. See text for details.

The nature of the scar states with large overlap with $|1\rangle$ states may be qualitatively understood by noting the form of $H_4^{(1)}$ given in Eq. (B5). For strong Δ', where the analysis of Ref. [52] holds, $H_4^{(1)}$ is the leading term in $1/\Delta'$ which induces spin dynamics. Here we note that such a term acting on a state $|1_j\rangle$ (which represents a single Rydberg excitation on the jth site) connects it to $|1_{j+2}\rangle$. Thus, it creates an almost closed subspace of $L/2$ such states; the corresponding Floquet eigenstates are therefore expected to have low entanglement and could be a candidate for the scar state having large overlap with $|1\rangle$.

A similar, but more complicated situation, holds for scars having large overlap with $|\mathbb{Z}_4\rangle$. We note that $H_4^{(1)}$ acting on $|\mathbb{Z}_4\rangle$ connects it to a series of $L/4$ states where any up-spin state is shifted by two sites. These states are denoted by $|\mathbb{Z}_{4j}\rangle$ and have repeated blocks of one up spin on site 4ℓ for integer ℓ and three subsequent down spins. Now let us consider the subsequent action of $H_4^{(1)}$ on this state; it is easy to see that a further shift of the jth up spin is either forbidden by the constraint or gives back $|\mathbb{Z}_4\rangle$. This ensures that action of $H_4^{(1)}$ on $|\mathbb{Z}_{4j}\rangle$ leads to $^{L/4}C_2$ new states. Following this argument we find that the dimension of the almost closed subspace
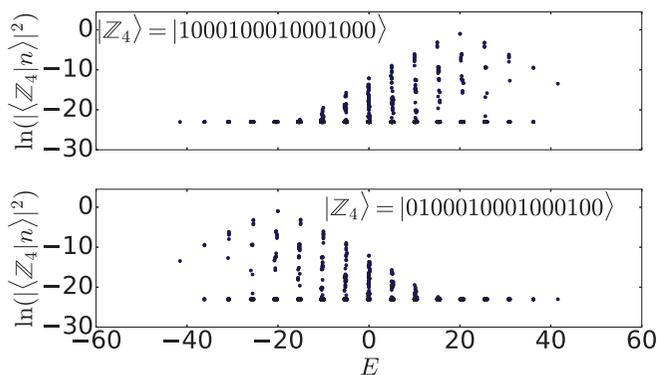
formed by the action of $H_4^{(1)}$ on $|\mathbb{Z}_4\rangle$ is $\sim \sum_{n=1\ldots L/4} {}^{L/4}C_n$. For finite $L \leqslant 24$ studied in our numerics, this leads to a small, almost closed, subspace of states. Thus, qualitatively one may expect to have a low-entangled eigenstate formed out of their superposition which has significant overlap with $|\mathbb{Z}_4\rangle$. We conjecture that such a state may be the Z_4 scar that we find. We also note that this suggests that scars having large overlap with $|1\rangle$ [for which the closed subspace always has O(L) states] would be more stable for large L than their counterparts having large overlap with $|\mathbb{Z}_4\rangle$.

VI. DISCUSSION

In this work, we have studied a periodically driven Rydberg chain with both uniform and staggered detuning. We have primarily focused on the limit of large drive amplitude and a square-pulse protocol; the uniform detuning term has been made time dependent. We have used FPT to obtain analytic insight for the Floquet Hamiltonian in the intermediate frequency regime. We note that for these interacting quantum systems, it is difficult to implement nonperturbative effective Hamiltonian techniques [8,76]; moreover, high-frequency expansions [8,73,74] do not provide an accurate description of the Floquet Hamiltonian in the intermediate frequency regime. This makes FPT our method of choice for obtaining analytic insight into the Floquet Hamiltonian; this choice is justified by a comparison of FPT-based results with exact numerics. We find that the presence of a staggered detuning term leads to several features of the driven system that have no analog in Floquet dynamics of Rydberg atoms without such a term.

The first of such features involves ergodicity violation of such system via clustering of Floquet eigenstates. We find that when $\Delta \gg w_r$, the eigenstates of the Floquet Hamiltonian arrange themselves into several discrete well-separated clusters in the Hilbert space. Each of these clusters belong to definite values of Z_π and the number of such clusters depends on the ratio of $\hbar \omega_D / \Delta_r$. We dub this phenomenon as primary clustering and recognize this to be a consequence of near integrability of H_F for large Δ_r / w_r. In addition, we also find a secondary clustering which leads to discrete set of states within each of these primary clusters. We tie the presence of such secondary clustering to the existence of emergent conserved quantity Y, which was noted earlier in the context of nondriven Rydberg chains with staggered detuning in Refs. [51,52]. We note that these clusterings leading to violation of ETH do not stem from standard Hilbert space fragmentation [57–60] since the Floquet Hamiltonian of the staggered Rydberg chain does not have dynamically disconnected sector at any finite w_r. Furthermore, such clustering is not expected to survive in the thermodynamic limit; however, they will be a feature of finite-sized chains which are typically realized in standard experiments [12,13].

We also show that the existence of Y and hence secondary clustering is contingent on incommensuration of the drive frequency and Δ_r which leads to a nonzero δE_2. Thus, at commensurate drive frequencies where $\delta E_2 = 0$, the secondary clustering is destroyed and states within each primary cluster become ergodic. This is reflected in the values of local observables such as O_{22} near these commensurate

FIG. 14. Plot of $\ln |\langle \mathbb{Z}_4 | n \rangle|^2$ as a function of E_F for $|\mathbb{Z}_4\rangle$ states which host Rydberg excitations on even (top panel) and odd (bottom panel) sites. For all plots $\Delta' = 5$ and $L = 16$. See text for details.

drive frequencies which reach very close to their ETH predicted values. This leads to a possibility of tuning ergodicity properties of the driven system using the drive frequency.

We also study the behavior of the correlation function O_{22} for the driven chain starting from the vacuum and the Neel states. We find, for initial $|0\rangle$ and $|\mathbb{Z}_2\rangle$, dynamical freezing of O_{22} at specific drive frequencies whose values are well approximated by the analytic Floquet Hamiltonian obtained using FPT. When driven close to these freezing frequencies, O_{22} starting from $|0\rangle$ or $|\mathbb{Z}_2\rangle$ displays oscillations with perfect revivals. The amplitude of these oscillations decreases with increasing Δ in the large or intermediate Δ/w_r regime; in contrast, their frequencies are pinned to $\Delta/\hbar$ for both the initial states. We provide a simple qualitative explanation of these features using the structure of the Floquet eigenstates in this regime. In contrast, such oscillations are completely suppressed when the dynamics starts from $|\bar{\mathbb{Z}}_2\rangle$; this leads to a range of drive frequencies where one encounters dynamic freezing. This range increases with Δ. We explain this phenomenon qualitatively in Appendix C and point out that the dynamics of O_{j2}, where j is odd, would show exactly opposite behavior: it would show range of freezing frequencies for dynamics starting from the $|\mathbb{Z}_2\rangle$ state. This dichotomy is a direct consequence of breaking of the sublattice symmetry by the staggered detuning term.

We have also studied the quantum scars in the Floquet eigenspectrum of such a driven Rydberg chain. Such scars are known to exist for $\Delta' = 0$ [33] and are dubbed as PXP scars [47]; they have identical overlap with both the Neel states in this limit. We find that with increasing Δ', the scars with energy $E_F < 0$ develop a stronger overlap with $|\mathbb{Z}_2\rangle$ while those with $E_F > 0$ overlap more with $|\bar{\mathbb{Z}}_2\rangle$. This phenomenon clearly originates from the breaking of the Z_2 sublattice symmetry due to presence of Δ. In fact, at large Δ', we find that no near mid-spectrum scar states have significant overlap with either of the Neel states. Instead, as confirmed from quench dynamics studies in Sec. V, they have a high overlap with either $|\mathbb{Z}_4\rangle$, vacuum ($|0\rangle$), or single-dipole ($|1\rangle$) states. This indicates that the presence of large Δ' leads to scars which have no analog with the standard PXP scars studied earlier in the literature. Our FSA analysis, detailed in Appendix D, explains the property of the scars at weak or intermediate Δ' fails to capture these mid-spectrum scars at large Δ'.

In conclusion, we have shown that a driven Rydberg chain with staggered detuning term leads to several interesting phenomena. These include ergodicity violation via Floquet eigenstate clustering in the strong staggered detuning limit, dynamical freezing, sustained coherent oscillations with perfect revivals near the freezing frequency, existence of separate class of quantum scars with large overlap with $|0\rangle$, $|1\rangle$, and $|\mathbb{Z}_4\rangle$ states, and the possibility of tuning ergodicity property of these chains with the drive frequency. The experimental implementation of a Rydberg chain has already been achieved [12,13]; a possible extension of some of these experiments with implementation of staggered detuning may provide a suitable experimental platform testing our theoretical predictions.

APPENDIX A: HIGHER-ORDER FPT TERMS

In this Appendix, we compute the higher-order corrections to the Floquet Hamiltonian within Floquet perturbation theory. It turns out that there is no second-order contribution to H_F since

$$U_2(T, 0) = -\int_0^T dt_1 U_0^\dagger(t_1, 0)(H_1 + H_2)U_0(t_1, 0)$$
$$\times \int_0^{t_1} dt_2 U_0^\dagger(t_2, 0)(H_1 + H_2)U_0(t_2, 0)$$
$$= U_1(T, 0)^2/2. \quad (A1)$$

Equation (A1) can be obtained from a straightforward computation; however, it can also be checked as follows. First, we note that the terms $\sim H_1$ in the expression of U_2 commute with U_0. This indicates that the term originating from H_1^2 in $U_2(T, 0)$ must trivially satisfy Eq. (A1). Second, we recall that it is known [32,33] that the term $\sim H_2^2$ does not yield any second-order contribution to H_F. This is due to the presence of a symmetry noted in Ref. [33]. For $\Delta = 0$, it was shown that $\{Q, H_F\} = 0$, where $Q = \prod_j \sigma_j^z$; consequently, there can be no terms with product of even number of $\tilde{\sigma}_j^\pm$ operators in H_F. Moreover, a straightforward computation shows that the contribution from all terms which involve both H_1 and H_2 also vanish due to commutation of H_1 with U_0. Thus, we have $H_F^{(2)} = 0$.

Next, we compute the third-order term in the Floquet Hamiltonian. To this end, we consider the third-order contribution to U, given by

$$U_3(T, 0) = i \int_0^T dt_2 U_0^\dagger(t_1, 0)(H_1 + H_2)U_0(t_1, 0)$$
$$\times \int_0^{t_1} dt_2 U_0^\dagger(t_2, 0)(H_1 + H_2)U_0(t_2, 0)$$
$$\times \int_0^{t_2} dt_2 U_0^\dagger(t_3, 0)(H_1 + H_2)U_0(t_3, 0). \quad (A2)$$

To obtain the third-order Floquet Hamiltonian, we first note that the commutation of H_1 with U_0 ensures that there is no third-order contribution to H_F from the term with three H_1 operators. The first nontrivial contribution to the third order H_F comes from the term in Eq. (A2) which has two H_1 and one H_2 operators. The contribution of this term to $U_3(T, 0)$ can be computed as charted in details in Ref. [32]. The result is

$$U_{3a}(T, 0) = \frac{i\Delta_0^2 w}{4} \sum_{j_1, j_2, j_3} \sum_{s=\pm} (-1)^{j_1+j_2} \big(2c_{1s}\sigma_{j_1}^z \sigma_{j_2}^z \tilde{\sigma}_{j_3}^s$$
$$+ c_{2s}\sigma_{j_1}^z \tilde{\sigma}_{j_3}^s \sigma_{j_2}^z\big),$$
$$c_{1\pm} = \pm T^3 \frac{-i \pm 2\gamma(1 \pm 2i\gamma) - ie^{\pm 2i\gamma}(2\gamma^2 - 1)}{32\gamma^3},$$
$$c_{2\pm} = \pm T^3 \frac{i \mp 2\gamma - ie^{\pm 2i\gamma}(2\gamma^2 + 1)}{16\gamma^3}. \quad (A3)$$

The structure of U_{3a} shows that it is necessary to categorize the terms into two groups. The first constitutes the case where at least one of the j_i's are different from the other two. For these, $U_{3a}(T, 0)$ either vanishes or can be written as

$$U_{3a}(T, 0) = \frac{i\Delta_0^2 w}{4} \sum_{j_1 \neq j_2 \neq j_3} \sum_{s=\pm} (-1)^{j_1+j_2}(2c_{1s} + c_{2s})$$

$$\times \sigma_{j_1}^z \sigma_{j_2}^z \tilde{\sigma}_{j_3}^s = \frac{U_1(T, 0)^3}{3!}, \quad \text{(A4)}$$

where we have used the fact that $2c_{1s} + c_{2s} = iT^2(\exp[i\lambda_0 Ts] - 1)/(\lambda_0 s)$ for $s = \pm 1$. Thus, such terms do not contribute to H_{F3}. However, when $j_1 = j_2 = j_3$, we find that the last term in Eq. (A3) acquires a negative sign due to the anticommutation of σ_j^z and $\tilde{\sigma}_j^s$. This leads to

$$U_{3a}(T, 0) = \frac{i\Delta_0^2 w}{4} \sum_j \sum_{s=\pm} (2c_{1s} - c_{2s})\tilde{\sigma}_j^s. \quad \text{(A5)}$$

Comparing this with $U_1(T, 0)^3/3!$, we find that there is a nontrivial contribution to the Floquet Hamiltonian given by

$$H_{F1}^{(3)} = \frac{w\Delta_0^2}{2T} \sum_j (c_{2+}\tilde{\sigma}_j^+ + \text{H.c.}). \quad \text{(A6)}$$

This term leads to a frequency-dependent renormalization of the coefficient of w in the first-order Floquet Hamiltonian.

The next contribution to the Floquet Hamiltonian comes from the terms in Eq. (A2) with two H_2 and one H_1 operators. The calculation of this term, $U_{3b}(T, 0)$, follows a similar route as that followed in Ref. [32] and leads to

$$U_{3b}(T, 0) = \frac{i\Delta_0 w^2}{2} \sum_{j_1, j_2, j_3} \sum_{s_1, s_2=\pm} (-1)^{j_3}(2d_{1s_1s_2}\tilde{\sigma}_{j_1}^{s_1}\tilde{\sigma}_{j_2}^{s_2}\sigma_{j_3}^z + d_{2s_1s_2}\tilde{\sigma}_{j_1}^{s_1}\sigma_{j_3}^z\tilde{\sigma}_{j_2}^{s_2}), \quad \text{(A7)}$$

$$d_{1++} = T^3 \frac{-(i/4 + \gamma) + ie^{2i\gamma}(i + 2\gamma) + e^{12i\gamma}(3i/4 + 2\gamma)}{32\gamma^3},$$

$$d_{1+-} = T^3 \frac{\gamma(2 - i\gamma) - \gamma e^{2i\gamma} - i(1 - e^{2i\gamma})/2}{16\gamma^3},$$

$$d_{2++} = T^3 \frac{i/4 - \gamma + 3e^{4i\gamma}/4 + e^{2i\gamma}(-i + 2\gamma)}{16\gamma^3}, \quad d_{2+-} = \frac{T^3}{8\gamma^3}\left(\frac{1}{2}\sin 2\gamma - \gamma\cos 2\gamma\right), \quad \text{(A8)}$$

and $d_{a\pm\pm} = d_{a\mp\mp}^*$ for $a = 1, 2$. The argument leading to the Floquet Hamiltonian is similar to the one discussed earlier and only the onsite terms in U_{3b} contribute to $H_F^{(3)}$. The final result is

$$H_{F2}^{(3)} = -\frac{w^2\Delta_0}{T} \sum_j (-1)^j(d_{2+-}\tilde{\sigma}_j^+ \sigma_j^z \tilde{\sigma}_j^- + \text{H.c.}). \quad \text{(A9)}$$

Note that the action of $H_{F2}^{(3)}$ on any eigenstate of σ_j^z is same as that of $-\sigma_j^z$. Thus, this term can be considered as a correction of the staggered detuning term in the first-order Floquet Hamiltonian. From Eq. (A7), we find that for $\tan 2\gamma > 2\gamma$, this correction is negative and leads to a reduction in the magnitude of the onsite detuning.

The final term in the Floquet Hamiltonian comes from the term in Eq. (A2) which has three H_2 operators. This term has already been computed in Ref. [32]; for completeness, we write the contribution of this term to H_F here. This is given by

$$H_{F3}^{(3)} = \sum_j A_0[(\tilde{\sigma}_{j-1}^+\tilde{\sigma}_{j+1}^+ + \tilde{\sigma}_{j+1}^+\tilde{\sigma}_{j-1}^+)\tilde{\sigma}_j^- - 6\sigma_j^+] + \text{H.c.},$$

$$A_0 = [e^{6i\gamma} + 3e^{2i\gamma}(1 + 4i\gamma) + 2(1 - 3e^{12i\gamma})]$$

$$\times \frac{w^3 T^2 e^{-12i\gamma}}{192 i\gamma^3}. \quad \text{(A10)}$$

This term contains a three-spin term as well as a higher-order correction to the first-order Floquet term $\sim w$.

This completes our derivation of the Floquet Hamiltonian for the driven Rydberg chain with staggered detuning to third order in Floquet perturbation theory. In subsequent sections, we shall use this along with numerical results to analyze the properties of the driven chain.

APPENDIX B: PROJECTION OPERATOR FORMALISM

In this Appendix, we detail the computation of Y and H_2 using a perturbative formalism developed in Ref. [52]. To this end we shall start from a Hamiltonian H_m [Eq. (17)] in the main text and treat $1/\Delta'$ as the perturbative parameter. In what follows, we write $H_m = H_0 + H_1$ [Eq. (17)], where

$$H_0 = -\Delta' Z_\pi, \quad H_1 = -\sum_j \tilde{\sigma}_j^x, \quad \text{(B1)}$$

and treat H_1 perturbatively in the regime where $\Delta' > 1$.

The formalism used in Ref. [52] constitutes construction of a perturbative effective Hamiltonian for such a system. The method relies on the presence of a canonical transformation, implemented through an operator S, which yields

$$H_{\text{eff}} = e^{iS} H_m e^{-iS} = H_0 + H^{(1)} + H^{(2)} + \cdots,$$

$$H^{(1)} = [iS, H_0] + H_1,$$

$$H^{(2)} = P'[iS, H_1] + \frac{1}{2}[iS, [iS, H_0]]P', \quad \text{(B2)}$$

where the ellipsis represents higher-order terms and P' is a projection operator which projects the Hamiltonian to the low-energy manifold of H_0 [52]. The next step is to determine

S to first order in perturbation theory by setting $H^{(1)} = 0$. A straightforward calculation using this condition yields

$$iS = \frac{1}{2i\Delta'}\sum_j \tilde{\sigma}_j^y (-1)^j. \tag{B3}$$

Using Eq. (B3), one can now compute $H^{(2)}$. While doing this, it is important to remember that the final results need to be projected in the low-energy manifold of H_0. This consideration leads to a single term in the second order which can be easily computed by substituting Eq. (B3) in (B2) given by

$$H^{(2)} = \frac{-1}{\Delta'}Y, \tag{B4}$$

where the expression of Y is given in Eq. (14) of the main text. We note that as long as the perturbation theory is valid, Y emerges as a constant of motion; however, this breaks down, along with the perturbative approach, when $\Delta' \to 0$.

The higher-order terms in the perturbation theory can be computed systematically using this approach and are detailed out in Ref. [52]. This yields $H^{(3)} = 0$; the leading-order nonzero term is given by $H^{(4)}$. As shown in Ref. [52], this can be written as

$$H^{(4)} = H_1^{(4)} + H_2^{(4)},$$

$$H_1^{(4)} = \frac{-1}{2\Delta'^3}\sum_j (-1)^j (\tilde{\sigma}_j^+ \tilde{\sigma}_{j+2}^- + \text{H.c.}),$$

$$H_2^{(4)} = \frac{-1}{2\Delta'^3}\sum_j P_{j-1}\sigma_j^z P_{j+1}P_{j+2} + P_{j-2}P_{j-}\sigma_j^z P_{j+1}$$
$$- 2P_{j-1}\sigma_j^z P_{j+1}. \tag{B5}$$

We note that $H_1^{(4)}$ is the leading-order term introducing non-trivial spin dynamics. The expression of $H_1^{(4)}$ has been used in Sec. V of the main text for developing a qualitative understanding of the $|\mathbb{Z}_4\rangle$ and single-dipole scar states.

APPENDIX C: OSCILLATIONS AROUND FREEZING FREQUENCIES

In this Appendix, we discuss the behavior of O_{22} around the freezing frequencies and provide a qualitative explanation of the difference of its time evolution starting from $|\mathbb{Z}_2\rangle$ and $|\bar{\mathbb{Z}}_2\rangle$ states. In the range of drive frequencies that we study here, $\Delta_r \simeq \Delta$ and we ignore their difference for the rest of this Appendix. The stroboscopic dynamics of O_{22} as a function of n around the freezing frequencies is shown in the top panel Fig. 15. We find that O_{22} does not thermalize; instead, it displays long-time oscillation with a fixed frequency $\omega_{\text{osc}} \simeq \Delta/\hbar$. We have checked this numerically for $n > 1000$ cycles. The amplitude $\mathcal{A}$ of these oscillations decreases as the freezing point is approached and also as Δ is increased; it is a monotonically decreasing function of w_r/Δ. However, the period of the oscillations remains constant for $\Delta/w \geqslant 1$, as shown in Fig. 16. A similar feature is seen from the fidelity $\mathcal{F} = |\langle \mathbb{Z}_2|\psi(nT)\rangle|^2$, where $|\psi(nT)\rangle$ denotes the many-body state at time $t = nT$, as shown in the bottom panel of Fig. 15. In contrast, the oscillation amplitude is close to zero for a wide range of frequencies around the freezing point when one starts from the $|\bar{\mathbb{Z}}_2\rangle$ state.
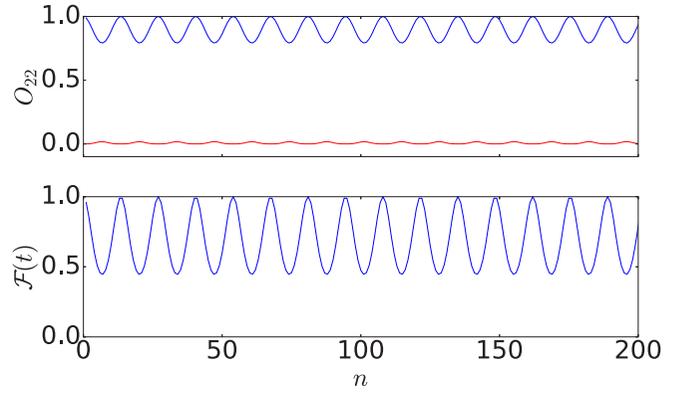
FIG. 15. Top panel: Plot of O_{22} as a function of the number of drive cycles n starting from the $|0\rangle$ (red line), $|\mathbb{Z}_2\rangle$ (black line). The bottom panel shows the plot of fidelity $\mathcal{F}$ as a function of n for $|\mathbb{Z}_2\rangle$ initial state. For all plots $L = 14$, $\lambda/w = 15$, and $\hbar\omega_D/w = 6.9$. All energies (frequencies) are scaled in units of w ($w/\hbar$). See text for details.

The characteristics of these oscillations at large Δ/w_r can be qualitatively understood as follows. Let us consider the evolution operator when $\Delta \gg w_r$. Clearly, in this limit, one can write

$$U(nT, 0) = \sum_\alpha e^{-in\epsilon_\alpha^F T/\hbar}|\alpha\rangle\langle\alpha|,$$

$$\epsilon_\alpha = E_0 + \alpha\Delta + O(w_r^2/\Delta^2),$$

$$|\alpha\rangle = \sum_p c_{p;q}^\alpha |p;q\rangle, \tag{C1}$$

where E_0 denotes the energy of the state $|0\rangle$ for $w_r = 0$ and any eigenstate $|\alpha = \alpha_0\rangle$ of the Floquet Hamiltonian H_F is mapped to a state in the number basis $|p;q\rangle = |p_0, q_0\rangle$ for $w_r = 0$. We note here that the states $|p_0; q_0\rangle$ have p_0 (q_0) up spins distributed on even (odd) sites of the chain without violation of the constraint; these are eigenstates of $H_F^{(1)}$ for $w_r = 0$ with quasienergy

$$E = E_0 + (q_0 - p_0)\Delta. \tag{C2}$$
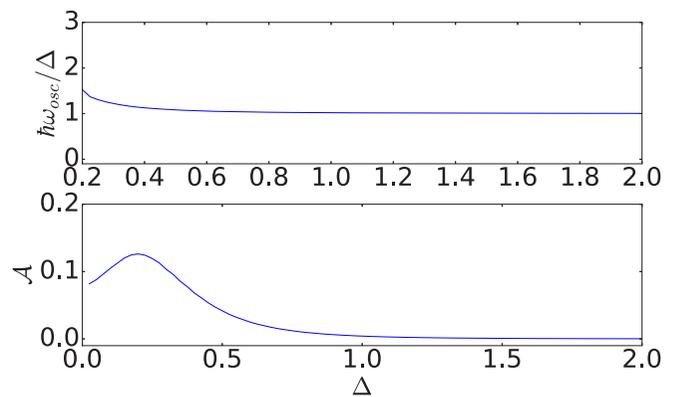
FIG. 16. Top panel: Plot of the frequency $\hbar\omega_{\text{osc}}/\Delta$ (top panel) and the amplitude $\mathcal{A}$ (bottom panel) of coherent oscillations of O_{22} as a function of Δ for $\hbar\omega_D/w = 6.9$ and $\lambda/w = 15$. All energies (frequencies) are scaled in units of w ($w/\hbar$). See text for details.

Here we shall assume that $c_{p_0+\mu;q_0}^{\alpha_0} \sim O[(w_r/\Delta)^{|\mu|}]$ for $\mu = \pm 1, \pm 2 \ldots$; thus, for small w_r/Δ, $|c_{p_0+\mu;q_0}^{\alpha_0}| \ll c_{p_0;q_0}^{\alpha_0}$ for any α_0. A similar relation holds for $c_{p_0;q_0+\mu}^{\alpha_0}$.

Let us now consider the initial state $|0\rangle$. The wave function after n drive cycles can be obtained as

$$|\psi(nT)\rangle = U(nT, 0)|0\rangle = \sum_\alpha c_{0;0}^{\alpha*} e^{-i\epsilon_\alpha nT/\hbar}|\alpha\rangle$$

$$= \sum_\alpha \sum_{p,q} c_{0;0}^{\alpha*} c_{p;q}^\alpha e^{-i\epsilon_\alpha pT/\hbar}|p;q\rangle, \qquad \text{(C3)}$$

where $c_{0;0}^\alpha = \langle p_0 = 0; q_0 = 0|\alpha\rangle$. Since the correlator O_{22} can receive finite contribution for states with $p_0 > 2$ up spins, we find that the leading contribution to O_{22} is given by

$$O_{22}^{(0)}(nT) \simeq |c_{0;0}^{0*} c_{2;0}^2 + c_{0;0}^{1*} c_{2;0}^1 e^{i\Delta nT/\hbar}|^2, \qquad \text{(C4)}$$

where we have retained only the leading-order term in w_r/Δ and used $\epsilon_{\alpha_0} \simeq E_0 - (p_0 - q_0)\Delta$ [Eq. (C1)]. This indicates that the oscillation amplitude $\mathcal{A}$ will decay with increasing Δ as $(w_r/\Delta)^4$; however, the frequency of these oscillations will be pinned to Δ as long as $w_r \ll \Delta$. The change in the oscillation frequency is expected to occur with reduction of Δ when $O[(w_r/\Delta)^2]$ terms in the expression of ϵ_α becomes significant. The validation of this argument can be found in Fig. 16. We note that for $\Delta \gg w_r$, the presence of a large onsite term which is diagonal in the Fock basis leads to long-time coherent oscillations; in this case, we do not find the rapid thermalization expected by ETH.

The coherent oscillations discussed above are expected to have larger amplitude provided we start from the state $|\mathbb{Z}_2\rangle$. To see this, we note that, in this case, the wave function after n drive cycles is given by

$$|\psi'(nT)\rangle = \sum_\alpha \sum_{p,q} c_{L/2;0}^{\alpha*} c_{p,q}^\alpha e^{-i\epsilon_\alpha nT/\hbar}|p;q\rangle, \qquad \text{(C5)}$$

where $c_{L/2;0}^\alpha = \langle \mathbb{Z}_2|\alpha\rangle$. In this case, the leading-order contribution to O_{22} reads as

$$O_{22}^{(\mathbb{Z}_2)}(nT) \simeq ||c_{L/2,0}^{L/2*}|^2 + c_{L/2,0}^{L/2-1*} c_{L/2-1,0}^{L/2-1} e^{i\Delta nT/\hbar}|^2 \qquad \text{(C6)}$$

which leads to $O(w_r^2/\Delta^2)$ oscillation amplitude.

In contrast, if one starts from the $|\bar{\mathbb{Z}}_2\rangle$ states, the oscillation amplitude is expected to be vanishingly small. This is due to the fact that $|\bar{\mathbb{Z}}_2\rangle$ has insignificant overlap with any $|p_0; q_0\rangle$ state which contributes to $\langle \hat{n}_2 \hat{n}_4 \rangle$. We also note that density-density correlation between odd sites (such as O_{12}) would show similar behavior for the initial state $|0\rangle$; however, it would have vanishing oscillation amplitude for the $|\mathbb{Z}_2\rangle$ initial state instead of $|\bar{\mathbb{Z}}_2\rangle$.

APPENDIX D: FSA-BASED ANALYSIS FOR SCARS AT SMALL Δ'

To understand the nature of these scars at low and intermediate Δ' and the change in their properties as Δ' is increased, we use a semianalytic FSA treatment. To this end, we first note that the presence of the staggered detuning term suggests that such a construction should distinguish between odd and even sites in the lattice. Therefore, we adapt the formalism of Ref. [75] which allows for such a sublattice-resolved formulation. In this method, the states are labeled by a set of

two integers n_1 and n_2 which denote number of Rydberg excitations (up spins) on even and odd sites, respectively. In what follows we shall construct the matrix elements of H_m between two such states and then diagonalize this matrix numerically. Such a class of states constitutes a symmetric subspace defined from a set of equivalence classes (n_1, n_2); all elements of these classes are invariant under shuffling of excitations in each sublattice [75]. Thus, in this scheme, the action of translation by an even number of lattice states leads to an equivalent state. The assumption here is that the key information about properties of the states resides in the number of excitations in each sublattice. We note that this procedure naturally yields states which have significant overlap with $|\mathbb{Z}_2\rangle$ and $|\bar{\mathbb{Z}}_2\rangle$ since these Neel states are included as elements in the subspace [75]. The first step towards construction of the matrix elements of H_m is to construct an orthonormal basis for the symmetric subspace. To this end, we use the prescription of Ref. [75] and write, for a chain with $2L$ sites,

$$|n_1, n_2\rangle = \frac{1}{\mathcal{N}} \sum_a |\alpha_a\rangle,$$

$$\mathcal{N} = \frac{(L - n_1 - n_2)L}{(L - n_1)(L - n_2)} \binom{L - n_1}{n_2} \binom{L - n_2}{n_1}, \quad \text{(D1)}$$

where any state $|\alpha_a\rangle$ contains n_1 and n_2 total Rydberg excitations on even and odd sites, respectively. The number of such states $\mathcal{N}$ depends on specific values of n_1 and n_2 and also on the Hilbert space constraint of having no two Rydberg excitations on neighboring sites.

The matrix element of H_m between these states can be easily obtained following the prescription of Ref. [75]. To this end, we write, using $|0\rangle$ as the reference state,

$$\langle n_1, n_2|H_m|m_1, m_2\rangle = F_1 + F_2,$$

$$F_1 = \Delta'(n_2 - n_1)\delta_{n_1,m_1}\delta_{n_2,m_2},$$

$$F_2 = -[M(n_1, n_2)\delta_{m_1,n_1+1}\delta_{m_2,n_2} \qquad \text{(D2)}$$

$$+ M(n_2, n_1)\delta_{m_1 n_1}\delta_{m_2,n_2+1}] + \text{H.c.},$$

$$M(n_1, n_2) = \sqrt{\frac{(L - n_1 - n_2)(L - n_1 - n_2 + 1)n_1}{L - n_1}}.$$

We note that the structure of the FSA Hamiltonian suggests that a large Δ' essentially separates out states with large n_1
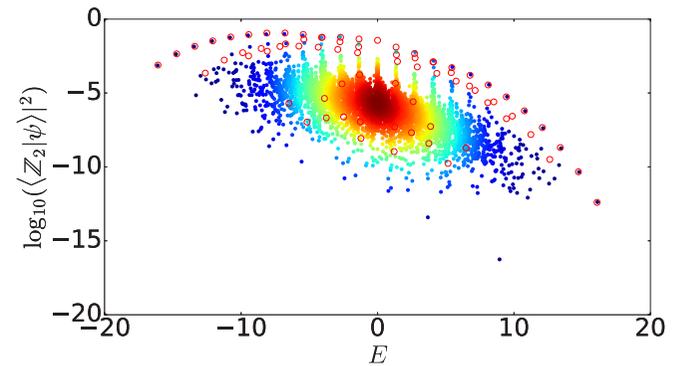
FIG. 17. A plot of $\log_{10}|\langle \mathbb{Z}_2|\psi\rangle|^2$ for states obtained via FSA (large red circles) and those obtained from exact numerics (small black circle) for $\Delta' = 0.5$ and $L = 24$. See text for details.
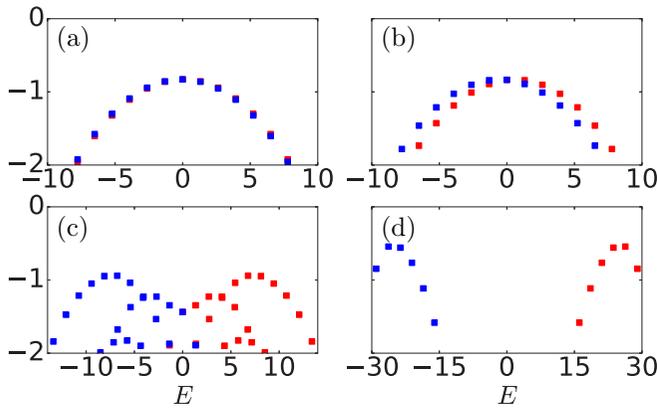
FIG. 18. A plot of $\log_{10}|\langle \mathbb{Z}_2|\psi\rangle|^2$ (blue circles) and $\log_{10}|\langle \bar{\mathbb{Z}}_2|\psi\rangle|^2$ (red circles) for states obtained via FSA for (a) $\Delta' = 0.005$, (b) 0.05, (c) 0.5, and (d) 2. All plots have same Y axes range and correspond to $L = 24$. See text for details.

from those with large n_2. Thus, the eigenvalues of this Hamiltonian, for large Δ', are expected to have large overlap with either $|\mathbb{Z}_2\rangle$ or $|\bar{\mathbb{Z}}_2\rangle$ but not both. The diagonalization of the FSA matrix constructed from Eq. (D2) leads to the eigenvalues of H_m for a fixed Δ'. A comparison of the $|\mathbb{Z}_2\rangle$ overlap of these states with those of their counterparts obtained via exact

numerics for $L = 24$ and $\Delta' = 0.5$, plotted in Fig. 17, shows a near-exact match between the scar eigenstates obtained by these two methods: the eigenstates with $E_F < 0$ have a much higher overlap with $|\mathbb{Z}_2\rangle$ compared to those with $E_F > 0$ in both cases. This allows us to surmise that the present FSA captures the essence of the scar eigenstates in the presence of finite Δ.

The overlap between these eigenstates with $|\mathbb{Z}_2\rangle$ (red dots) and $|\bar{\mathbb{Z}}_2\rangle$ (blue dots) is shown in Fig. 18. From these, we find that the FSA eigenstates qualitatively reproduce the characteristics of scars seen in exact numerics. For low Δ', the scar states have near-exact overlap with both the Neel states (top left panel of Fig. 18); in contrast, as Δ' is increased, states with $E_F > 0$ develop a large overlap with $|\bar{\mathbb{Z}}_2\rangle$ while those with $E_F < 0$ overlap strongly with $|\mathbb{Z}_2\rangle$. Thus, the crossover of the nature of the scars as a function of Δ' is well captured by the FSA. This behavior can be understood to be a consequence of the presence of the diagonal elements of the FSA matrix for finite Δ' [Eq. (D2)]; their presence pushes states having large overlap with $|\mathbb{Z}_2\rangle$ ($|\bar{\mathbb{Z}}_2\rangle$) to opposite ends of the Floquet spectrum. The mid-spectrum scar states at large Δ', however, can not be captured by the present FSA formalism. A more detailed quantitative understanding of such states and their description in terms of a modified FSA approach is left for future studies.

[1] A. Polkovnikov, K. Sengupta, A. Silva, and M. Vengalattore, Rev. Mod. Phys. **83**, 863 (2011).

[2] J. Dziarmaga, Adv. Phys. **59**, 1063 (2010).

[3] A. Dutta, G. Aeppli, B. K. Chakrabarti, U. Divakaran, T. F. Rosenbaum, and D. Sen, *Quantum Phase Transitions in Transverse Field Spin Models: From Statistical Physics to Quantum Information* (Cambridge University Press, Cambridge, 2015).

[4] S. Mondal, D. Sen, and K. Sengupta, in *Quantum Quenching, Annealing and Computation*, edited by A. Das, A. Chandra, and B. K. Chakrabarti, Lecture Notes in Physics Vol. 802 (Springer, Berlin, 2010), p. 21; C. De Grandi and A. Polkovnikov, in *Quantum Quenching, Annealing and Computation*, edited by A. Das, A. Chandra, and B. K. Chakrabarti, Lecture Notes in Physics Vol. 802 (Springer, Berlin, 2010), p. 75.

[5] M. Bukov, L. D'Alessio, and A. Polkovnikov, Adv. Phys. **64**, 139 (2015).

[6] L. D'Alessio and A. Polkovnikov, Ann. Phys. **333**, 19 (2013).

[7] L. D'Alessio, Y. Kafri, A. Polokovnikov, and M. Rigol, Adv. Phys. **65**, 239 (2016).

[8] A. Sen, D. Sen, and K. Sengupta, J. Phys.: Condens. Matter **33**, 443003 (2021).

[9] I. Bloch, J. Dalibard, and W. Zwerger, Rev. Mod. Phys. **80**, 885 (2008); L. Tarruell and L. Sanchez-Palencia, C. R. Phys. **19**, 365 (2018).

[10] M. Greiner, O. Mandel, T. Esslinger, T. W. Hänsch, and I. Bloch, Nature (London) **415**, 39 (2002); C. Orzel, A. K. Tuchman, M. L. Fenselau, M. Yasuda, and M. A. Kasevich, Science **291**, 2386 (2001).

[11] T. Kinoshita, T. Wenger, and D. S. Weiss, Nature (London) **440**, 900 (2006); L. E. Sadler, J. M. Higbie, S. R. Leslie, M. Vengalattore, and D. M. Stamper-Kurn, *ibid.* **443**, 312 (2006).

[12] W. Bakr, J. Gillen, A. Peng, S. Foelling, and M. Greiner, Nature (London) **462**, 74 (2009); W. S. Bakr, A. Peng, M. E. Tai, R. Ma, J. Simon, J. I. Gillen, S. Folling, L. Pollet, and M. Greiner, Science **329**, 547 (2010).

[13] H. Bernien, S. Schwartz, A. Keesling, H. Levine, A. Omran, H. Pichler, S. Choi, A. S. Zibrov, M. Endres, M. Greiner, V. Vuletic, and M. D. Lukin, Nature (London) **551**, 579 (2017); H. Levine, A. Keesling, A. Omran, H. Bernien, S. Schwartz, A. S. Zibrov, M. Endres, M. Greiner, V. Vuletic, and M. D. Lukin, Phys. Rev. Lett. **121**, 123603 (2018).

[14] T. Kitagawa, E. Berg, M. Rudner, and E. Demler, Phys. Rev. B **82**, 235114 (2010); N. H. Lindner, G. Refael, and V. Galitski, Nat. Phys. **7**, 490 (2011); T. Kitagawa, T. Oka, A. Brataas, L. Fu, and E. Demler, Phys. Rev. B **84**, 235108 (2011).

[15] M. Thakurathi, A. A. Patel, D. Sen, and A. Dutta, Phys. Rev. B **88**, 155133 (2013); A. Kundu, H. A. Fertig, and B. Seradjeh, Phys. Rev. Lett. **113**, 236803 (2014).

[16] F. Nathan and M. S. Rudner, New J. Phys. **17**, 125014 (2015); B. Mukherjee, A. Sen, D. Sen, and K. Sengupta, Phys. Rev. B **94**, 155122 (2016); B. Mukherjee, P. Mohan, D. Sen, and K. Sengupta, *ibid.* **97**, 205415 (2018).

[17] T. Nag, S. Roy, A. Dutta, and D. Sen, Phys. Rev. B **89**, 165425 (2014); T. Nag, D. Sen, and A. Dutta, Phys. Rev. A **91**, 063607 (2015).

[18] A. Agarwala, U. Bhattacharya, A. Dutta, and D. Sen, Phys. Rev. B **93**, 174301 (2016); A. Agarwala and D. Sen, *ibid.* **95**, 014305 (2017).

[19] D. J. Luitz, Y. Bar Lev, and A. Lazarides, SciPost Phys. **3**, 029 (2017); D. J. Luitz, A. Lazarides, and Y. Bar Lev, Phys. Rev. B **97**, 020303(R) (2018).

[20] R. Ghosh, B. Mukherjee, and K. Sengupta, Phys. Rev. B **102**, 235114 (2020).

[21] M. Heyl, A. Polkovnikov, and S. Kehrein, Phys. Rev. Lett. **110**, 135704 (2013); M. Heyl, Rep. Prog. Phys. **81**, 054001 (2018).

[22] A. Sen, S. Nandy, and K. Sengupta, Phys. Rev. B **94**, 214301 (2016); S. Nandy, K. Sengupta, and A. Sen, J. Phys. A: Math. Theor. **51**, 334002 (2018); M. Sarkar and K. Sengupta, Phys. Rev. B **102**, 235154 (2020).

[23] S. Aditya, S. Samanta, A. Sen, K. Sengupta, and D. Sen, Phys. Rev. B **105**, 104303 (2022); A. A. Makki, S. Bandyopadhyay, S. Maity, and A. Dutta, *ibid.* **105**, 054301 (2022).

[24] V. Khemani, A. Lazarides, R. Moessner, and S. L. Sondhi, Phys. Rev. Lett. **116**, 250401 (2016).

[25] D. V. Else, B. Bauer, and C. Nayak, Phys. Rev. Lett. **117**, 090402 (2016).

[26] J. Zhang, P. W. Hess, A. Kyprianidis, P. Becker, A. Lee, J. Smith, G. Pagano, I.-D. Potirniche, A. C. Potter, A. Vishwanath, N. Y. Yao, and C. Monroe, Nature (London) **543**, 217 (2017).

[27] A. Das, Phys. Rev. B **82**, 172402 (2010).

[28] S. Bhattacharyya, A. Das, and S. Dasgupta, Phys. Rev. B **86**, 054410 (2012).

[29] S. S. Hegde, H. Katiyar, T. S. Mahesh, and A. Das, Phys. Rev. B **90**, 174407 (2014).

[30] S. Mondal, D. Pekker, and K. Sengupta, Europhys. Lett. **100**, 60007 (2012).

[31] U. Divakaran and K. Sengupta, Phys. Rev. B **90**, 184303 (2014).

[32] B. Mukherjee, A. Sen, D. Sen, and K. Sengupta, Phys. Rev. B **102**, 075123 (2020).

[33] B. Mukherjee, S. Nandy, A. Sen, D. Sen, and K. Sengupta, Phys. Rev. B **101**, 245107 (2020).

[34] S. Nandy, A. Sen, and D. Sen, Phys. Rev. X **7**, 031034 (2017).

[35] S. Nandy, A. Sen, and D. Sen, Phys. Rev. B **98**, 245144 (2018).

[36] B. Mukherjee, A. Sen, D. Sen, and K. Sengupta, Phys. Rev. B **102**, 014301 (2020).

[37] J. M. Deutsch, Phys. Rev. A **43**, 2046 (1991).

[38] M. Srednicki, Phys. Rev. E **50**, 888 (1994); J. Phys. A: Math. Gen. **32**, 1163 (1999).

[39] M. Rigol, V. Dunjko, and M. Olshanii, Nature (London) **452**, 854 (2008).

[40] L. D'Alessio and M. Rigol, Phys. Rev. X **4**, 041048 (2014).

[41] D. M. Basko, I. L. Aleiner, and B. L. Altshuler, Ann. Phys. **321**, 1126 (2006).

[42] R. Nandkishore and D. A. Huse, Annu. Rev. Condens. Matter Phys. **6**, 15 (2015).

[43] F. Alet and N. Laflorencie, C. R. Phys. **19**, 498 (2018).

[44] D. A. Abanin, E. Altman, I. Bloch, and M. Serbyn, Rev. Mod. Phys. **91**, 021001 (2019).

[45] D.-L. Deng, S. Ganeshan, X. Li, R. Modak, S. Mukerjee, and J. H. Pixley, Ann. Phys. **529**, 1600399 (2017).

[46] C. J. Turner, A. A. Michailidis, D. A. Abanin, M. Serbyn, and Z. Papic, Nat. Phys. **14**, 745 (2018).

[47] C. J. Turner, A. A. Michailidis, D. A. Abanin, M. Serbyn, and Z. Papic, Phys. Rev. B **98**, 155134 (2018).

[48] K. Bull, I. Martin, and Z. Papic, Phys. Rev. Lett. **123**, 030601 (2019).

[49] V. Khemani, C. R. Laumann, and A. Chandran, Phys. Rev. B **99**, 161101(R) (2019).

[50] S. Moudgalya, N. Regnault, and B. A. Bernevig, Phys. Rev. B **98**, 235156 (2018).

[51] T. Iadecola, M. Schecter, and S. Xu, Phys. Rev. B **100**, 184312 (2019).

[52] I.-C. Chen and T. Iadecola, Phys. Rev. B **103**, 214304 (2021).

[53] N. Shiraishi, J. Stat. Mech. (2019) 083103.

[54] M. Schecter and T. Iadecola, Phys. Rev. B **98**, 035139 (2018).

[55] P. A. McClarty, M. Haque, A. Sen, and J. Richter, Phys. Rev. B **102**, 224303 (2020).

[56] D. Banerjee and A. Sen, Phys. Rev. Lett. **126**, 220601 (2021).

[57] S. Pai, M. Pretko, and R. M. Nandkishore, Phys. Rev. X **9**, 021003 (2019); V. Khemani, M. Hermele, and R. Nandkishore, Phys. Rev. B **101**, 174204 (2020).

[58] P. Sala, T. Rakovszky, R. Verresen, M. Knap, and F. Pollmann, Phys. Rev. X **10**, 011047 (2020); S. Moudgalya, A. Prem, R. Nandkishore, N. Regnault, and B. A. Bernevig, arXiv:1910.14048.

[59] Z.-C. Yang, F. Liu, A. V. Gorshkov, and T. Iadecola, Phys. Rev. Lett. **124**, 207602 (2020); G. De Tomasi, D. Hetterich, P. Sala, and F. Pollmann, Phys. Rev. B **100**, 214313 (2019).

[60] B. Mukherjee, D. Banerjee, K. Sengupta, and A. Sen, Phys. Rev. B **104**, 155117 (2021).

[61] S. Coleman, R. Jackiw, and L. Susskind, Ann. Phys. **93**, 267 (1975).

[62] S. Coleman, Ann. Phys. **101**, 239 (1976).

[63] S. Chandrasekharan and U. J. Wiese, Nucl. Phys. B **492**, 455 (1997); U. J. Wiese, Ann. Phys. (Amsterdam) **525**, 777 (2013).

[64] E. Zohar, I. I. Cirac, and B. Reznik, Rep. Prog. Phys. **79**, 014401 (2016).

[65] R. Brower, S. Chandrasekharan, and U. J. Wiese, Phys. Rev. D **60**, 094502 (1999); R. Brower, S. Chandrasekharan, S. Riederer, and U. Wiese, Nucl. Phys. B **693**, 149 (2004).

[66] M. Dalmonte and S. Montangero, Contemp. Phys. **57**, 388 (2016).

[67] D. Banerjee, M. Dalmonte, M. Müller, E. Rico, P. Stebler, U.-J. Wiese, and P. Zoller, Phys. Rev. Lett. **109**, 175302 (2012); D. Banerjee, M. Bogli, M. Dalmonte, E. Rico, P. Stebler, and U. J. Wiese, and P. Zoller, *ibid.* **110**, 125303 (2013).

[68] A. Celi, B. Vermersch, O. Viyuela, H. Pichler, M. D. Lukin, and P. Zoller, Phys. Rev. X **10**, 021057 (2020).

[69] A. J. A. James, R. M. Konik, and N. J. Robinson, Phys. Rev. Lett. **122**, 130603 (2019).

[70] F. M. Surace, P. P. Mazza, G. Giudici, A. Lerose, A. Gambassi, and M. Dalmonte, Phys. Rev. X **10**, 021041 (2020).

[71] S. Sachdev, K. Sengupta, and S. M. Girvin, Phys. Rev. B **66**, 075128 (2002).

[72] P. Fendley, K. Sengupta, and S. Sachdev, Phys. Rev. B **69**, 075106 (2004).

[73] N. Goldman and J. Dalibard, Phys. Rev. X **4**, 031027 (2014).

[74] A. Eckardt and E. Anisimovas, New J. Phys. **17**, 093039 (2015).

[75] C. J. Turner, J.-Y. Desaules, K. Bull, and Z. Papic, Phys. Rev. X **11**, 021021 (2021).

[76] J. C. Sandoval-Santana, V. G. Ibarra-Sierra, J. L. Cardoso, A. Kunold, P. Roman-Taboada, and G. Naumis, Ann. Phys. **531**, 1900035 (2019).